

High-Resolution Flow-Simulation in Typhoon 21, 2018: Massive Loss of Submerged Macrophytes in Lake Biwa

Satoshi Nakada (✉ nakada.satoshi@nies.go.jp)

National Institute for Environmental Studies: Kokuritsu Kankyo Kenkyujo <https://orcid.org/0000-0001-5391-1690>

Hiroki Haga

Lake Biwa Museum

Maho Iwaki

National Institute for Environmental Studies: Kokuritsu Kankyo Kenkyujo

Keisuke Hatano

Japan Water Agency

Kohji Mabuchi

National Institute for Environmental Studies: Kokuritsu Kankyo Kenkyujo

Noriko Takamura

National Institute for Environmental Studies: Kokuritsu Kankyo Kenkyujo

Research article

Keywords: flow-simulation, typhoon, submerged macrophytes, Lake Biwa, fluid force

Posted Date: December 29th, 2020

DOI: <https://doi.org/10.21203/rs.3.rs-134971/v1>

License: © ⓘ This work is licensed under a Creative Commons Attribution 4.0 International License.

[Read Full License](#)

Version of Record: A version of this preprint was published at Progress in Earth and Planetary Science on August 16th, 2021. See the published version at <https://doi.org/10.1186/s40645-021-00440-9>.

1
2
3 **High-resolution flow-simulation in Typhoon 21, 2018:**
4 **massive loss of submerged macrophytes in Lake Biwa**
5
6
7
8
9
10

11 NAKADA Satoshi ¹ (nakada.satoshi@nies.go.jp)
12 HAGA Hiroki ² (haga-hiroki@biwahaku.jp)
13 IWAKI Maho ^{1,2} (iwaki.maho@nies.go.jp)
14 HATANO Keisuke ³ (keisuke_hatano@water.go.jp)
15 MABUCHI Kohji ¹ (mabuchi.koji@nies.go.jp)
16 TAKAMURA Noriko ¹ (noriko-t@nies.go.jp)
17
18
19

20 1) National Institute for Environmental Studies, 16-2 Onogawa, Tsukuba, Ibaraki, 305-8506, Japan.

21 TEL: +81-29-850-2883; FAX: +81-29-850-2569

22 2) Lake Biwa Museum, 1091 Oroshimo-cho, Kusatsu, Shiga, 525-0001, Japan

23 TEL: +81-77-568-4811; FAX: +81-77-568-4850

24 3) Japan Water Agency, 2-1-10 Katata, Otsu, Shiga, 520-0243, Japan

25 TEL: +81-77-574-0680; FAX: +81-77-574-1739
26
27

28 *Corresponding author: Satoshi. NAKADA

29 TEL: +81-29-850-2883; FAX: +81-29-850-2569

30 E-mail: nakada.satoshi@nies.go.jp
31

32 **Keywords:** flow-simulation, typhoon, submerged macrophytes, Lake Biwa, fluid force

33 **Running head:** Outflow simulation of aquatic plant by typhoon
34
35

36

37

38

Abstract

39

40 Global activities of typhoons and hurricanes are gradually changing, and these storms can drastically affect lake
41 ecosystems through the recession of submerged macrophytes that regulate the water quality in lakes. Using an
42 echosounder, we captured the short-term, massive loss of submerged macrophytes attributed to the abnormal
43 fluctuation of the water level induced by the approach of a catastrophic super typhoon in the south basin of Lake
44 Biwa, Japan. This paper investigates the physical processes responsible for the loss of vegetation using a high-
45 resolution circulation model in Lake Biwa as a pilot study area. The circulation model was coupled with
46 dynamical models of the fluid force and erosion acting on the vegetation. Our simulation successfully
47 reproduced the water level fluctuation and high-speed current (torrent) generated by the typhoon gale. The
48 simulated results demonstrate that the fluid force driven by the gale-induced torrent uprooted submerged
49 macrophytes during the typhoon approach and that this fluid force (rather than erosion) caused the outflow of
50 vegetation. As a result, this uprooting attributed to the fluid force induced the massive loss of submerged
51 macrophytes in a large area of the south basin, which might have increased primary production and reduced the
52 stock of fish such as bluegill in the lake. Our approach is practical for evaluating changes in lake environments
53 attributed to the massive outflow of submerged macrophytes under various climate change scenarios. (227
54 words)

55

56 **Declaration**

57

58

59 **Availability of data and materials**

60 Please contact author for data requests.

61

62

63 **Funding**

64 This work was supported by the Collaborative Research Fund from Shiga Prefecture “Studies on conservation
65 and ecosystem management of Lake Biwa” under the Japanese Grant for Regional Revitalization.

66

67

68 **Competing interests**

69 The authors declare that they have no competing interests.

70

71

72 **Authors' contributions**

73 SN mainly contributed to writing paper, modeling, simulation, data analysis. HH contributed to the
74 observation of the plant height of macrophytes by an echosounder. MI contributed to the in-situ data collection
75 and analysis of time series of the water level. KH contributed to the observational meteorological data such as
76 wind and air pressure. KM contributed to the in-situ data collection of time series of the water level at various
77 sites. NT mainly contributed to study design of this paper and many discussions.

78

79

80

81

82

83 **1. Introduction**

84 Global activities of tropical storms (typhoons and hurricanes), which can drastically affect wetland and lake
85 ecosystems, are gradually changing. Moreover, tropical storms disturb the community structures of aquatic
86 plants in tropical and temperate regions (Wang et al., 2016). Many lakes in these regions are within the strike
87 zones of tropical storms, and they experience highly interseasonal and interannual variations in rainfall and
88 runoff (Havens et al., 2016). With future warming of the tropical sea surface based on prediction model results,
89 the Intergovernmental Panel on Climate Change (IPCC, 2007) reported that tropical cyclones will become more
90 intense, leading to more violent winds and rainfall.

91 Aquatic plants, particularly submerged macrophytes, play an important role in aquatic environments by
92 positively interacting with the water quality and ecosystems of lakes. The submerged macrophytes in shallow
93 eutrophic lakes can affect nutrient cycling, sediment–water interactions, water column irradiance, and
94 phytoplankton blooming (Weisner et al., 1997). The vegetation of submerged macrophytes supplies a variety of
95 ecosystem functions, providing shelters for fish and aquatic invertebrates, restoring water quality, and regulating
96 the oxygen balance (Sood et al., 2012). Accordingly, recent studies have focused on the phytoremediation and
97 purification effects of submerged macrophytes on nutrient-polluted water (e.g., Sood et al., 2012; Yanran et al.,
98 2012, Dhote and Dixit, 2017).

99 The ecosystem in a shallow lake can change drastically during the short-term approach of a storm coincident
100 with the recession of aquatic plants. Ji et al. (2018) reported that a lake disturbed by tropical storms experienced
101 a regime shift from clear to turbid water by losing submerged vegetation. Heavy rainfall, flooding, and strong

102 winds can also create suitable habitats for aquatic organisms and increase their diversity in regions frequently
103 affected by typhoons (Wang et al., 2008).

104 To understand the short-term changes taking place within a lake ecosystem, we need to know the physical
105 processes that induce the large-scale recession of aquatic plants; unfortunately, no analysis has been performed
106 to reinforce this knowledge. Damage to aquatic plants varies based on the life forms of species, geological
107 habitat conditions, and tropical storm intensity (Wang et al., 2016). For example, tropical storms cause damage
108 to mangroves, including the loss of foliage, breakage of trunks, and even uprooting of trees (Ellison, 1998).
109 However, little is known about the process by which submerged macrophytes disappear during tropical storms.
110 This lack of knowledge exists because no biological data that would be useful for analyzing the disappearance
111 of submerged macrophytes are available from both before and after a typhoon strike.

112 As a consequence, a simulation coupled with flow and dynamical models on high-resolution grids is needed
113 to analyze the dissipation of submerged macrophytes; in addition, observational data are needed to describe the
114 loss of vegetation. The use of a high-resolution flow model can be a powerful approach for simulating the
115 massive loss of submerged macrophytes. To date, various models have been proposed for simulating lake
116 circulation (e.g., Akitomo et al., 2009), water temperature and the thermocline (e.g., Koue et al., 2018), dissolved
117 oxygen (Kitazawa et al., 2010), primary production (Sato et al., 2011), and other features at the seasonal and
118 interannual time scales; nevertheless, the grid resolutions of these models are insufficient for representing the
119 detailed flow field with a focus on submerged macrophytes. In this context, previous studies proposed a
120 theoretical framework and bulk models for the fluid force acting on submerged macrophytes (e.g., Luhar and

121 Nepf, 2017; Hayashi and Konno, 2007). Fortunately, we succeeded in collecting observational plant height data,
122 which are necessary for capturing the massive loss of submerged macrophytes, by conducting echosounder
123 surveying on a regular schedule.

124 This paper investigates the short-term, massive loss of submerged macrophytes as a result of the approach
125 of a catastrophic super typhoon in Lake Biwa, Japan, which is taken as a pilot study area (Figure 1). We
126 identified the key physical factors governing this massive loss using a numerical fluid simulation coupled with
127 an evaluation of the fluid force and erosion models focusing on the habitats of submerged macrophytes in the
128 lake. To investigate the processes that caused the outflow of vegetation, we proposed two dynamical models,
129 namely, erosion of the bed and the fluid force acting on the vegetation body, leading to the uprooting of
130 submerged macrophytes. In the first model, the outflow can be induced by erosion generated by a strong current
131 or torrent (Figure 2a). In the second model, the outflow can be induced by the fluid force generated by the
132 torrent (Figure 2b).

133

134

135 **2. Study area**

136 Lake Biwa (Figure 1) is the largest lake in Japan (with a volume of 27.5 km^3), providing water resources for
137 approximately 14.5 million people in the Kansai region (e.g., the Shiga, Kyoto, Osaka, and Hyogo regions),
138 including some megacities. The lake, which has a surface area of 670 km^2 , is located on the central island of the
139 Japanese archipelago, Honshu. Lake Biwa consists of two basins, a deep north basin (area-mean depth of 44 m,

140 maximum depth of 104 m) and a shallow south basin (area-mean depth of 4 m); the latter, which represents our
141 study field, has a surface area of 51.6 km² (Haga, 2006). The lake water is generally provided by more than 100
142 rivers in the watershed (3174 km²) and is discharged through a single outlet (Kawanabe et al. 2012), namely,
143 the Seta River in the south, under the control of a weir to regulate the runoff and water level of the lake. In
144 recent years, extensive beds of submerged macrophytes have developed in the south basin. Over the last two
145 decades, submerged macrophytes covered over 90% of the area of the south basin (Haga and Ishikawa, 2016).

146

147

148 **3. Methods and data**

149 **3.1 Model**

150 We evaluated the key factors of the above processes by following the procedure of the flow chart shown in
151 Figure 3; we coupled a circulation model with two dynamical models to represent the outflow of submerged
152 macrophytes described in Section 2. We simulated the large-scale changes in the lake water level induced by
153 Typhoon 21 using an unstructured-grid ocean model and atmospheric reanalysis data. Then, the shear stress and
154 fluid force acting on flexible plants were calculated based on bed shear stress theory and a hydraulic resistance
155 model.

156

157 **3.1.1 Lake circulation model**

158 In the simulation part of the flowchart (Figure 3), we used the prognostic, unstructured-grid Finite-Volume

159 Community Ocean Model (FVCOM) (Chen et al., 2003). This finite-volume approach ensures the conservation
160 of the mass and heat necessary to reproduce the key physical processes under a dominant change in the water
161 level of the lake. The FVCOM uses an unstructured, terrain-following triangular grid, leading to an improved
162 flexibility in adjusting the grid resolution (10-60 m) to fit the irregular coastal geometry and bathymetry of Lake
163 Biwa (Figure 4). A σ -z mixed coordinate system consisting of five constant-thickness (0.5 m) layers in the
164 surface layer and a 10 sigma layer below the surface was employed in the vertical dimension to represent the
165 realistic temperature stratification.

166 Considering the observed large fluctuation in the water level induced by Typhoon 21 (explained in detail in
167 Section 4.2), the simulation was conducted for a week following the approach of Typhoon 21 to the lake on 4
168 September 2018. The ocean simulations with a time interval of 0.2 seconds began from an initial state of rest
169 and lasted for 2 weeks with a start date of 29 August 2018.

170

171 **3.1.2 Input data to the circulation model**

172 Four input datasets, namely, bathymetry, water temperature, runoff, and meteorological reanalysis datasets,
173 were used in the simulation, as shown by the flowchart (Figure 3). We used bathymetry data with a 50 m
174 horizontal resolution (Figure 1c and 1d) distributed by the Lake Biwa Environmental Research Institute
175 (LBERI) of Shiga Prefecture as the input data to the simulation and interpolated these data to the unstructured
176 grids in the FVCOM (Figure 4). The in situ temperature data observed on 28 August at Imadu-oki-Chuou (Figure
177 1c) obtained by LBERI were used as the initial water temperature conditions in the simulation and were

178 homogeneously input to our model horizontally.

179 The hourly mean river discharges from the Seta River used in the simulation (Figure 1d) were observed at
180 the Seta River Weir operated by the Ministry of Land, Infrastructure, Transport and Tourism (MLIT) of Japan,
181 Kinki Regional Development Bureau Biwako Office. The daily mean river discharges used in the simulation
182 were similarly determined from the precipitation accumulated in each watershed area (Nakada et al., 2017). The
183 derived discharges were validated using the runoff data estimated by the observed water levels, for example, at
184 the Takatoki River (at Nodera-bashi).

185 Reanalysis meteorological Grid Point Value datasets of the Meso-Scale Model (GPV-MSM) produced by
186 the Japan Meteorological Agency were downloaded from the server of the Research Institute for the Sustainable
187 Humanosphere (<http://database.rish.kyoto-u.ac.jp/arch/jmadata/>) and input into the FVCOM as the mean hourly
188 air pressure at the land surface, air temperature at 2 m, precipitation, cloud cover, relative humidity, and wind
189 velocity at 10 m produced by inter/extrapolation using a Gaussian function.

190

191 **3.1.3 Erosion estimation**

192 A conceptual model (Figure 2a) exhibiting the concepts underlying the calculation of the nondimensional
193 bed shear stress, sediment resuspension, and the flux of sediment from the lakebed to lakewater was employed
194 in similar simulations (e.g., Nakada et al., 2018). The nondimensional bed shear stress, R_τ , at each computational
195 grid was obtained from the following equations:

$$196 \quad R_\tau = \tau_b / \tau_e - 1 \quad (1),$$

197
$$\tau_b (= \rho_w u^2) \quad (2),$$

198
$$\tau_e (= 0.79\tau_y^{0.94}) \quad (3),$$

199 where τ_b is the bed shear stress and τ_e is the critical shear stress. When $\tau_b > \tau_e$, or in other words, $R_\tau > 0$,
 200 bed sediment can be transported from the seabed into the lake water. Here, ρ_w (1000 kg m^{-3}) is the density of
 201 lake water, and $u = \sqrt{gn^2U^2/D^{1/3}}$ is the bottom friction velocity, which is determined by the gravitational
 202 acceleration constant g (9.8 m s^{-2}), the roughness coefficient n (0.025), the current speed U , and the total
 203 depth D ($=h+H$). Here, h is the water depth, and H is the water level. $\tau_y = 1.494 \times 10^6 \omega^{-2.452}$ is the yield
 204 value, which is determined by the moisture ratio of the bed sediment $\omega = W/(1 - W)$ or the moisture content
 205 W (Figure 5). Values of W were produced by inter/extrapolation to the computational grid using a Gaussian
 206 function based on sediment observations by the Lake Biwa Museum in 2002 (Haga et al., 2006). The south
 207 basin has a maximum W of 81% and higher W values than the areas around the Karasuma Peninsula (Figure 1c)
 208 and the entrance of the Seta River ($W < 60\%$). The instantaneous erosion (or resuspended sediment flux) from
 209 the bed $E(t)$ ($\text{kg m}^{-2} \text{ s}^{-1}$) of each grid in the model domain of the south basin (Figure 4b) was calculated using
 210 the following empirical equation (see Umita et al., 1988; Nakano et al., 1991; Otsubo and Muraoka, 1985 for
 211 the physical parameters used in the equation):

212

213
$$E(t) = MR_\tau^{2.3} \quad (4),$$

214

215 where M ($= 1.6 \times 10^{-5}$) is the resuspension constant ($\text{kg m}^{-2} \text{ s}^{-1}$) and t is an arbitrary time in the model. The total

216 erosion induced by bed flow is calculated as follows:

$$217 \quad E_T = \int_{t_s}^{t_e} E(t) dt \quad (5).$$

218

219 **3.1.4 Fluid force acting on submerged macrophytes**

220 To evaluate the fluid force, we employed the general theoretical model for buoyant, flexible macrophyte
221 blades in flow (Figure 2b) (e.g., Luhar and Nepf, 2017). In this paper, we employed a few simplifying
222 assumptions without the flow-induced reconfiguration of buoyant, flexible vegetation to evaluate the outflow
223 of the submerged macrophytes (Hayashi and Konno, 2007). 1) The blades of the submerged macrophytes, such
224 as *Vallisneria*, were modeled as isolated, buoyant, inextensible elastic stems with a constant representative width
225 ($b=0.01$ m), thickness ($t=0.001$ m), and density ($\rho_v=160$ kg m⁻³). 2) The horizontal velocity (U) was uniform
226 over depth and had a steady flow; the dominant hydrodynamic force was form drag, and unsteady flows, such
227 as those induced by surface waves, were not considered. 3) Viscous skin friction was negligible. Form drag,
228 which is derived from the velocity normal to the blade surface, was represented using a standard quadratic law.

229 The drag force acting on a blade length equivalent to the plant height h_v is:

$$230 \quad F_D = (1/2)\rho_w C_D b h_v U^2 \cos^2 \theta \quad (6).$$

231

232 Here, ρ_w (1000 kg m⁻³) is the density of lake water and C_D (1.7) is the drag coefficient (Hayashi and
233 Konno, 2007). The blade length is given by the observed macrophyte height shown in Section 4.1. Hayashi and
234 Konno (2007) evaluated the local bending angle θ (Figure 2b) of the blade relative to the vertical ($0^\circ \leq \theta \leq$

235 90° , where $\theta=0^\circ$ denotes an upright posture) based on laboratory experiments. Following their blade model

236 based on the moment balance, as shown in Figure 5b, the drag force is:

237
$$F_D = F_B \sin\theta \quad (7).$$

238

239 Here, the vertical buoyancy force is:

240
$$F_B = (\rho_w - \rho_v) g t b h_v \quad (8),$$

241

242 and g (9.8 m s^{-2}) is the gravitational acceleration constant. The fluid force acting on the blade induced by

243 the flow and buoyancy is:
$$F_F = F_B \cos\theta \quad (9).$$

244

245 From equations (6) and (7):

246
$$F_B \sin\theta = (1/2) \rho_w C_D b h_v U^2 \cos^2\theta. \quad (10).$$

247

248 Solving equation (10), we can obtain the following solution:

249
$$\sin\theta = (-F_B + \sqrt{F_B^2 + \psi^2})/\psi \quad (11),$$

250
$$\cos\theta = F_B \sqrt{2(\sqrt{(1 + (F_B/\psi)^2} - 1))/\psi} \quad (12).$$

251 Here, $\psi = \rho_w C_D b h_v U^2$. Therefore, the fluid force can be derived using the simulated current velocity U and

252 the observed macrophyte height h_v :

253
$$F_F = F_B^2 \sqrt{2(\sqrt{(1 + (F_B/\psi)^2} - 1))/\psi} \quad (13).$$

254 In this fashion, we calculated the fluid force F_F at each model time step and evaluated the outflow of the
255 submerged macrophytes from the bed.

256

257 **3.2. Data**

258 **3.2.1 Plant height data**

259 We used the plant height data of submerged macrophytes derived by echosounding surveys conducted on a
260 regular schedule in the pretyphoon period (on 9 and 10 August 2018) and in the posttyphoon period (on 5, 6,
261 and 12 September). The observation configuration was composed of a BioSonics MX Echosounder system
262 (BioSonics Inc.), which was used to measure the plant heights, and a differential-GPS (d-GPS) WU800 device
263 (Japan Radio, Co., Ltd., Tokyo, Japan) for positioning. The transducer of the echosounder was installed in the
264 bottom of a vessel hull and positioned 0.3 m under water. The echosounding surveys, which were capable of
265 covering the vegetation distribution in the south basin, were conducted along 30 longitudinal transects spaced
266 at intervals of 500 m at a vessel speed of 9-13 km/hour (5-7 knots), as shown in Figure 1d.

267 The raw data derived by the echosounder were processed by Visual Habitat (BioSonics Inc.) to detect the
268 lake bottom and the submerged macrophytes based on the default detection configuration, although we manually
269 modified the configuration as appropriate. The detection limit for plant heights was set to 0.1 m. The processed
270 data, formatted by comma-separated values (CSV), were interpolated by inter/extrapolation into the triangular
271 grids of the FVCOM (Figure 4) using a Gaussian function (Nakada and Isoda, 2000). The grid datasets were
272 used to calculate the difference in the plant heights between the pre- and posttyphoon periods and to estimate

273 the fluid force acting on the macrophytes using the plant height h_v based on equations (6-9).

274

275 **3.2.2 Water level and chlorophyll-a data**

276 Figure 1c shows the observation stations operated by the MLIT, the Japan Water Agency (JWA), and the
277 Lake Biwa Branch Office of the National Institute for Environmental Studies. In situ water level data were used
278 to verify the simulated water level to ensure the reproducibility of the model. The MLIT releases real-time,
279 observational data on the water level at gauge stations. The water level data were downloaded from the website
280 of the Water Information System run by the MLIT (<http://www1.river.go.jp/>) with an analysis period
281 corresponding to the span of the simulated data to allow a comparison of the in situ data with the simulated
282 water level data. We used meteorological data, such as wind, water level, and chlorophyll-a data, and water
283 quality data observed at the Ogoto offshore comprehensive automatic observation station operated by the JWA.
284 Due to the potential for the biofouling of in-water instrumentation, the sensors were maintained by the JWA at
285 a regular semimonthly interval. We also collected hourly data of the water level at three stations (Figure 1c)
286 using HOBO U20L-02 water level loggers (Onset Computer Corporation, USA).

287

288

289 **4. Results**

290 **4.1. Massive loss of submerged macrophytes**

291 Figure 6 displays the observed height of the submerged macrophytes on 9 August 2018, as measured by the

292 onboard echosounder, which indicates that there was a substantial area of submerged macrophytes in the south
293 basin. The submerged macrophyte beds (36.4 km²) covered 68% of the area of the south basin, and the area-
294 mean height was 0.54 m.

295 The approach of Typhoon 21 might have induced the large-volume outflow of submerged macrophytes and
296 short-term blooms of phytoplankton over a large area of the south basin. On 4 September 2018, category 5 super
297 Typhoon 21 (Jebi) approached Lake Biwa at 15:00 JST (Figure 1a) and induced a south-to-southeast gale in the
298 surface layer (Figure 1b). After the typhoon approach, the submerged macrophyte height on 5 September
299 significantly decreased throughout the whole basin (area-mean height 0.23 m) with a 58% height reduction
300 compared to the area-mean height before Typhoon 21; in particular, the vegetation height was nearly zero in the
301 southern area of the basin. A map of the difference in macrophyte height (Figure 6c) shows an average decrease
302 in the submerged macrophyte height (0.31 m) and a reduction in the coverage area of 18.8 km², which
303 constituted 53% of the south basin. The area in which the height decreased accounted for 35.2 km², which was
304 97% of the area of the inherent habitat of the submerged macrophytes. Furthermore, significant decreases in
305 height occurred in three areas: the north-central area of the basin, the nearshore area along the eastern coast, and
306 the estuarine area around the old Kusatsu River. After the reduction in the area of submerged macrophytes, on
307 5 September, the concentration of chlorophyll-a in the south basin nearly doubled relative to the concentration
308 during the pretyphoon period between 1 and 3 September (Figure 7) although the peaks on 4 September might
309 imply the benthic algal resuspension.

310

311 4.2 Model validation

312 4.2.1 Wind data used in the simulation

313 Figure 8a shows the time series of the area-averaged wind vector over the model domain of the south basin
314 of Lake Biwa. A southeast wind was dominant at noon on 3 September; this condition changed from a strong
315 south wind to a southwest wind when the typhoon approached Lake Biwa. A map of the wind speeds and vectors
316 is illustrated in Figure 8b at 15:00 JST on 4 September (red line in Figure 8a); when Typhoon 21 was
317 approaching, Lake Biwa was characterized by a strong south wind with a homogeneous horizontal distribution
318 over the lake. The wind speed increased northward and exceeded 28 m/s in the northern area of the south basin.

319 Figure 8c shows a scatter plot between the GPV-MSM-predicted wind speed and the in situ wind speed
320 observed at the Ogoto offshore observation station (Figure 1c) during the period of 3-6 September, although
321 some data are missing at 15:00 and 16:00 JST on 4 September. The comparison between the observed and
322 predicted wind speeds in this scatterplot suggests that the observed speed was approximately 2 times larger than
323 the predicted speed, leading to the derivation of a wind estimation formula (modified wind $W_{mod} =$
324 $1.89W_{MSM}$) from the predicted wind W_{MSM} with a high correlation coefficient ($R=0.92$). Following the derived
325 formula, we modified the wind speed in the simulation as an input.

326

327 4.2.2 Water level fluctuation

328 Figure 9a shows the time series of the observed and simulated water levels during the typhoon approach
329 period on 4 September. Both time series at the southern observational site (Mihogasaki) indicate that the

330 predominant decreases (approximately 1 m) in the water level were induced by typhoon winds. On the other
331 hand, the water levels of both time series at the northern observational site (Katayama) increased by
332 approximately 20 cm when the water level at the southern site was at a local minimum.

333 A comparison between the observed and simulated water levels at all observational sites (Figure 9b) results
334 in a high correlation coefficient ($R=0.94$, $N=246$) and a low calculation error ($RMSE=12.15$ cm, $BIAS=-5.35$
335 cm) compared to the magnitude of the water level change. This suggests that the calculated water levels of the
336 simulation results are reasonably reproducible. Thus, the FVCOM simulation was capable of qualitatively
337 reproducing the water level fluctuations induced by typhoon winds.

338

339

340 **4.3. Simulated results**

341 **4.3.1 Gale-induced torrent**

342 Figure 10 shows three snapshots of the simulated water level distribution (color shading) and surface flow
343 field (vectors) in the south basin during the typhoon approach, indicating the generation of a gale-induced torrent.
344 The northward torrent induced by the south-southeast wind exceeded 1 m/s in the northern area during 15:00-
345 16:00 JST but was larger than the flow speed in the southern area. The water level was reduced by approximately
346 1.2 m due to the massive water transport associated with the northward torrent; consequently, the water level in
347 the southern area was significantly lower than that in the northern area. On the other hand, after the south winds
348 of the typhoon diminished (Figure 11), the water level recovered to approximately 0 m during 17:00-19:00 JST.

349 The temporal variation of the surface currents indicates that the southward backwash currents returned from the
350 north basin, and their speed exceeded 1 m/s in the northern area; moreover, the speed of these currents in the
351 northern area was greater than that in the southern area at 18:00 JST when southward water transport was
352 dominant.

353 Figure 12 shows maps of the maximum speeds and vectors of the surface and bottom currents. The
354 horizontal pattern of the maximum current speed at the surface indicates that the northward current was
355 dominant during the typhoon period. The maximum speed of the northern area was larger than that of the
356 southern area and was particularly dominant but localized in the narrow strait around the Biwako-ohashi Bridge.
357 The pattern of the maximum speed of the bottom current shows that the southward current was dominant in the
358 direction opposite to that of the surface flow pattern. The dominant maximum bottom speed was also limited in
359 the most northern area near the Biwako-ohashi Bridge.

360 Figure 13 shows the time series of the area-averaged water level (black solid line) in the south basin (up to
361 north of $35^{\circ} 7.8' N$); a prominent negative peak of the water level is visible at 16:10. The area-averaged flow
362 speed at the surface shows two prevalent peaks of 0.83 and 0.51 m/s at 15:10 and 17:20 JST, respectively; these
363 apparent fluctuations suggest the to-and-fro transport of a large volume of $3.64 \times 10^{10} \text{ m}^3$ (= water level difference
364 of 0.71 m \times water area of the south basin of 51.6 km²) between the south and north basins. Three peaks of the
365 bottom speed were visible at 14:00, 15:20, and 16:40 JST during the typhoon approach period (12:00-18:00
366 JST); the maximum peak (0.25 m/s) of the bottom flow was reached first, and its magnitude was approximately
367 one-third that of the maximum peak of the surface flow. The temporal variation of the surface flow speed was

368 similar to that of the depth- and area-averaged flow speed in the south basin (blue solid line), suggesting that
369 the surface velocity field represented the flow dynamics in the south basin. In contrast, the temporal variation
370 after 20:00 indicates that small fluctuations occurred after the typhoon departed the area.

371

372 **4.3.2 Erosion**

373 Figure 14 shows the maps used to evaluate the shear stress and erosion induced by the torrent at the bed.
374 The map of the critical shear stress (Figure 14a) derived by equation (3) shows the highest values in the
375 northeastern area around the coast of the Karasuma Peninsula and in the southern area near the Ohmi-ohashi
376 Bridge. These areas have a relatively low water content. Figure 14b shows a map of the time-averaged bed shear
377 stress during the period of 2-5 September obtained by equation (2); this map indicates a large stress ($>0.5 \text{ N/m}^2$)
378 in the northern area, particularly in the strait area near the Biwako-ohashi Bridge. These areas presented a larger
379 bed stress than the areas exhibiting the dominant speed of bottom flow (Figure 12). Moreover, the values in the
380 southern area were substantially small, ranging from 0 to 0.4 N/m^2 , except for the higher values at the head of
381 the southern outlet flowing into the Seta River.

382 Based on the results of the critical and bed shear stresses (Figure 14a and 14b), we derived a map of the
383 time-averaged nondimensional bed shear stress \underline{R}_τ (Figure 14c) during the period of 2-5 September on the basis
384 of equation (1). The \underline{R}_τ value was nearly zero and displayed a similar pattern to the bed shear stress (Figure
385 14b), indicating a larger \underline{R}_τ in the northern area, particularly in the strait area. Hence, the bed shear stress
386 associated with substantial erosion is expected to be small.

387 As a result of the nondimensional bed shear stress distribution, we derived a map of the total or time-
388 integrated erosion E_T defined by equation (5) during the period of 2-6 September (Figure 14d). This map
389 indicates that the value of the erosion was nearly zero, except for the higher erosion (> 5 cm) in the northernmost
390 strait area. This suggests that most erosion was limited in the northernmost strait area according to the
391 distribution pattern of \underline{R}_τ (Figure 14c); this distribution is similar to the area with a high bed shear stress (Figure
392 14b). Consequently, the magnitude of the bottom flow speed determined the magnitude of the nondimensional
393 bed shear stress related to erosion.

394

395 4.3.3 Fluid force

396 We estimated the distribution of the fluid force F_F using the flow velocity based on equation (13) and
397 created maps of the maximum F_F and time-averaged magnitude of the fluid force \widehat{F}_F during the period of 2-6
398 September (Figure 15). The spatial pattern of the time-averaged \widehat{F}_F was similar to that of the maximum F_F ;
399 both patterns presented larger values in the north-central area, in the western coastal area, and in the estuarine
400 area of the Kusatsu River. These patterns mirrored the spatial pattern of the decrease in height of submerged
401 macrophytes (Figure 2c), suggesting that the fluid force induced by the torrent could have uprooted the
402 submerged macrophytes with the greatest heights and washed them out.

403 Figure 16 shows the time series of the area-averaged magnitude of the fluid force \widehat{F}_F and the
404 nondimensional bed shear stress \widehat{R}_τ in the south basin. The temporal variation of \widehat{F}_F was also predominant
405 during the typhoon approach period and showed three peaks, although the first peak was small. The variation

406 in \widehat{F}_F was closer to that in the surface flow than to that in the bottom flow and remained large after the typhoon
407 approach (Figure 13). The temporal variation of \widehat{R}_τ exhibited three peaks during the typhoon approach period;
408 these peaks corresponded to those of the bottom flow speed (Figure 13), illustrating that the magnitude of \widehat{R}_τ
409 was dominated by the magnitude of the bottom flow speed. Subsequently, the magnitude of \widehat{R}_τ rapidly
410 diminished after the third peak and decreased to nearly zero after 18:00 JST.

411

412

413 **5. Discussion**

414 This paper highlights that the fluid force (rather than erosion) driven by a gale-induced torrent during the
415 approach of a typhoon at Lake Biwa uprooted the submerged macrophytes therein, leading to the massive
416 outflow of those macrophytes from a large area of the south basin of Lake Biwa. These results demonstrate that
417 a previously proposed theoretical framework (e.g., Luhar and Nepf, 2011) and analytical model (Hayashi and
418 Konno, 2007) are applicable even to the high flow speed range of 1 m/s or larger for calculating the fluid force
419 acting on submerged macrophytes. Our approach can contribute to assessing the damage to and erosion risk of
420 aquatic populations in various lakes (Chiu et al., 2017), particularly in lakes with aquatic macrophyte habitats,
421 during storm strikes worldwide (Short et al. 2016). In particular, based on an evaluation considering violent,
422 high-intensity typhoon strikes projected under climate change scenarios (Mei and Xie, 2016), we can estimate
423 the frequency at which submerged macrophytes will experience massive losses in the future. These findings are
424 expected to lead to an understanding of lake ecosystems and the creation of adaptation strategies to cope with

425 projected climate change with respect to short-term events attributed to typhoon strikes (Jeppesen et al., 2017).

426 The massive loss of submerged macrophytes could decrease the fish stock. In fact, the bluegill (*Lepomis*
427 *macrochirus*) in Lake Biwa, the population of which is decreasing interannually with a rapid decreasing
428 tendency, reached a minimum level in 2019, as shown by the fish catch data archived in the Shiga Prefecture
429 website (<https://www.pref.shiga.lg.jp/ippan/kankyoshizen/biwako/307015.html>). This may be attributable to the
430 short-term, typhoon-induced, drastic decrease in the submerged macrophyte bed since submerged macrophytes
431 can provide a habitat for invertebrates and act as feeding sites and refugia for bluegill (Miller et al., 2018). Cross
432 and McNerny (2005) reported that these changes in the submerged plant cover and its detritus substrates can
433 primarily explain the spatial variation of the bluegill abundance. According to Schriver et al. (1995), changes in
434 the abundance of submerged macrophytes can impact fish-zooplankton-phytoplankton interactions in shallow
435 eutrophic lakes.

436 The reproducibility of our simulation results depends on the accuracy of the wind and current velocity data,
437 which is a limitation of our approach. We evaluated the accuracy of the simulated water level compared with
438 the observed water level (RMSE: 0.12 m); this value falls within 9% of the water level amplitude (approximately
439 1.4 m) of both the observed and the simulated fluctuations, suggesting sufficient reproducibility in analyses of
440 the fluctuations generated by a typhoon gale. Note that the accuracy of the wind estimation at the lake surface
441 can largely contribute to the reproducibility of our flow simulation and depends on the observational error of
442 the wind observations. Both the wind speed and the wind direction can significantly affect the fetch in the south
443 basin and the intensity of the gale-induced torrent. The accuracy of our simulation could decline without the

444 validation of the GPV-MSM-predicted wind based on observational data of the lake surface wind. The fluid
445 force model used in the simulation is simple because the fluid force is determined by two variables (input data)
446 for the simulated current speed driven mainly by the lake surface wind and the observed plant height. We verified
447 the validity of the simulated results based on observational data of the water level, suggesting that a limitation
448 of our model is that the accuracy of the simulated current velocity is unknown. The current velocity must be
449 observed in the areas with submerged macrophyte beds for a comparison with the simulated velocity to improve
450 the accuracy of the simulated speed.

451 The wind-induced wave may also contribute to wave-induced current generating fluid force and the bed
452 shear stress acting on erosion, resulting in macrophyte uprooting. We evaluated the representative wave height
453 H_w (=0.5 m) and period T_w (=2.2 sec.) during the typhoon approach period of 14:00-19:00 JST on 4 September
454 based on the simple SMB method (Bretschneider, 1970) using the observed wind speeds (14.5-19.6 m/s) and
455 supposing the typical fetches (3-4 km). Considering the area-mean depth D (=4 m) of the south basin and wave
456 length $L_w = gT_w^2/(2\pi)$ (=7.5 m), we obtained scale criterion $D/L_w > 1/2$, indicating that the wind wave
457 induced by the typhoon-gale was the deep water wave. The orbital of the deep wave water is exponentially
458 decreased, and its half-excursion near the bottom approximately takes $e^{-D}H_w$ as well as the orbital velocity.
459 As a result, we derived the typical wave-induced current $U_b = 2\pi e^{-D}H_w/T_w$ (=0.03 m/s) near the bottom based
460 on the similar calculation (Dufois et al., 2008). The current speed of U_b was smaller than that of the torrent-
461 induced current as shown in Figure 12, suggesting that the effect of wind waves is negligible. Therefore, the
462 wind-induced wave and wave-induced current can secondary contribute to the erosion and fluid force.

463 This study illustrates that a high-resolution grid of several tens of meters is highly suitable to reproduce the
464 current velocity induced by a typhoon strike. Our model is composed of grids with a high horizontal resolution
465 (10-60 m), as shown in Figure 6, which corresponds to the longitudinal resolution of the echosounder
466 observation system used to measure the vegetation height of the submerged macrophytes (Figure 1d). This
467 resolution can contribute to a reasonable calculation of the fluid force acting on the submerged macrophytes
468 using a realistically simulated water level and flow in the south basin. In comparison, a model using a coarser
469 spatial resolution than that of our model experienced difficulty simulating the high-speed currents generated by
470 an atmospheric disturbance and was therefore insufficient (Nakada et al., 2014). To date, the grid resolutions of
471 previously proposed models were larger than 0.5 km because the main purpose of those models was to reproduce
472 the lake circulation associated with the seasonal thermocline and the interannual variations of the lake water
473 temperature (e.g., Akitomo et al., 2009; Koue et al., 2018). We first employed a flow model with a regular 0.5
474 km grid to simulate the gale-induced current, but the reproducibility of the water level was insufficient for our
475 analyses (not shown).

476 The massive outflow of submerged macrophytes induced by storm strikes can drastically change the lake
477 ecosystem and environment, which should be investigated with respect to climate change scenarios (Jeppesen
478 et al., 2017). A southwest wind larger than 20 m/s blew during the study period for longer than 3 hours (Figure
479 8), inducing a northward torrent and volumetric transport from the south basin to the north basin (Figure 10 and
480 11). We confirmed that the concentration of chlorophyll-a in the south basin after the typhoon approach nearly
481 doubled relative to the concentration during the pretyphoon period between 1 and 3 September (Figure 3). This

482 suggests that short-term blooms of toxic cyano harmful algal bloom (HAB) species might occur over a large
483 area of the south basin once the turbidity has declined, as indicated by Haven et al. (2016). Typhoons will be
484 more intense and violent under the future projected climate of East Asia (Mei and Xie, 2016), which could
485 increase the possibility of events that generate a variety of consequences such as massive losses and rapid
486 increases in HABs. Similar problems can be shared among the many global lakes with submerged macrophyte
487 vegetation. We suggest the analysis of typhoon strikes focusing on various lakes at a worldwide scale based on
488 regional climate change scenarios to enable the exploration of possible drastic changes in lake environments
489 triggered by the massive loss of submerged macrophytes.

490

491

492 **6. Conclusions**

493 This study examined the massive loss of submerged macrophytes induced by a super typhoon and
494 investigated the physical processes responsible for the outflow of vegetation using a high-resolution flow model.
495 The simulated results demonstrated that the fluid force driven by a gale-induced torrent uprooted the submerged
496 macrophytes during the typhoon approach; this fluid force (rather than erosion) was the mechanism responsible
497 for the removal of macrophytes. As a result, these processes induced the massive loss of submerged macrophytes
498 over the large area of the south basin of Lake Biwa.

499 The proposed high-resolution flow model will be essential for evaluating the short-term, massive losses
500 induced by typhoon strikes, although the reproducibility of the simulation depends on the accuracy of the wind.

501 The massive outflow of submerged macrophytes induced by storm strikes can drastically change the ecosystem
502 and environment of a lake, leading to a possible reduction in the fish stock and an increase in primary production.
503 Our simulation successfully reproduced the abnormal fluctuation of the water level generated by the typhoon
504 gale. The model accuracy of our flow simulation using high-resolution grids was acceptable for the fluid force
505 analysis and did not affect our conclusion. We hope that such drastic changes attributed to the massive outflow
506 of submerged macrophytes will be investigated based on climate change scenarios.

507
508
509
510

511 **Acknowledgements**

512 This work was supported by the Collaborative Research Fund from Shiga Prefecture “Studies on conservation
513 and ecosystem management of Lake Biwa” under the Japanese Grant for Regional Revitalization. We thank Dr.
514 C. Jiao, Lake Biwa Environmental Research Institute, Shiga, Japan for providing the bathymetry grid data of
515 Lake Biwa. In this research work we used the supercomputer of ACCMS, Kyoto University. We thank the
516 Research Institute for Sustainable Humanosphere, Kyoto University for providing the input datasets of GPV-
517 MSM.

518
519

References

- 520
521
522 Akitomo K., K. Tanaka M. and M. Kumagai. 2009. Annual cycle of circulations in Lake Biwa, part 2:
523 mechanisms. *Limnology* 10:119–129, DOI 10.1007/s10201-009-0268-6
- 524 Bretschneider, C. L. 1970. Wave forecasting relations for wave generation. *Look Lab, Hawaii*, 1(3).
- 525 Chen C., H. Liu, and R. C. Beardsley. 2003. An unstructured grid, finite-volume, three dimensional, primitive
526 equations ocean model: application to coastal ocean and estuaries. *J. Atmos. Ocean Technol.* 20(1): 159–186.
- 527 Chiu Y.-T., A. Bain, S.-L. Deng, Y.-C. Ho, W.-H. Chen, and H.-Y. Tzeng. 2017. Effects of climate change on a
528 mutualistic coastal species: Recovery from typhoon damages and risks of population erosion. *PLoS ONE*
529 12(10):e0186763, doi: 10.1371/journal.pone.0186763
- 530 Cross T. K., and M. C. McInerny. 2005. Spatial Habitat Dynamics Affecting Bluegill Abundance in Minnesota
531 Bass–Panfish Lakes. *North American Journal of Fisheries Management*, 25(3):1051–1066, DOI
532 10.1577/M04-072.1
- 533 Dhote S., and S. Dixit. 2009. Water quality improvement through macrophytes—a review. *Environ Monit*
534 *Assess* 152:149–153, DOI 10.1007/s10661-008-0303-9
- 535 Dufois F., P. Garreau, P. Le Hir, and P. Forget. 2008. Wave-and current-induced bottom shear stress distribution
536 in the Gulf of Lions. *Continental Shelf Research* 28(15): 1920–1934.
- 537 Ellison J.C. 1998. Impacts of Sediment Burial on Mangroves. *Marine Pollution Bulletin* 37(8–12): 420–426.
- 538 Haga H. 2006. Confirmation of surface area of the southern basin of Lake Biwa, Japan. *Japanese Journal of*
539 *Limnology* 67:123–126 [in Japanese].
- 540 Haga H., T. Ohtsuka, M. Matsuda, and M. Ashiya. 2006. Spatial distributions of biomass and species
541 composition in submerged macrophytes in the southern basin of Lake Biwa in summer of 2002. *Japanese*
542 *Journal of Limnology* 67:69–79. [in Japanese]
- 543 Haga H., and K. Ishikawa. 2016. Spatial distribution of submerged macrophytes in the southern Lake Biwa
544 basin in the summer of 2014, in comparison with those in 2002, 2007 and 2012. *Japanese Journal of*
545 *Limnology* 77(1):55–64, doi.org/10.3739/rikusui.77.55
- 546 Havens K., H. Paerl, E. Philips, M. Zhu, J. Beaver, and A. Srifa. 2016. Extreme Weather Events and Climate
547 Variability Provide a Lens to How Shallow Lakes May Respond to Climate Change. *Water* 8(229):1–18,
548 doi:10.3390/w8060229
- 549 Hayashi K., and M. Konno. 2007. Fluid forces and hydraulic resistance by plants deforming and oscillating in
550 river flow, *Proceedings of hydraulic engineering* 51:1231–1236, [in Japanese] doi.org/10.2208/prohe.51.1231
- 551 IPCC. 2007. Summary for policymakers, in S. Solomon, D. Qin, M. Manning, Z. Chen, M. Marquis, K. B.
552 Averyt, M. Tignor, and H. L. Miller [eds.], *Climate Change 2007; The Physical Science Basis. Contribution*
553 *of Working Group I to the Fourth Assessment Report of the Intergovernmental Panel on Climate Change*,
554 Cambridge University Press.
- 555 Ji G., K. E. Havens, J. R. Beaver, T. and L. East. 2018. Recovery of plankton from hurricane impacts in a large
556 shallow lake. *Freshwater Biology* 63:366–379, doi.org/10.1111/fwb.13075
- 557 Jeppesen E, M. Søndergaard, and Z. Liu. 2017. *Lake Restoration and Management in a Climate Change*

558 Perspective: An Introduction. *Water* 9(2):122, doi:10.3390/w9020122

559 Kawanabe H., M. Nishino, and M. Maehata. 2012. *Lake Biwa: interactions between nature and people*. Springer.

560 Kitazawa D., M. Kumagai, and N. Hasegawa. 2010. Effects of Internal Waves on Dynamics of Hypoxic Waters
561 in Lake Biwa. *Journal of the Korean Society for Marine Environment and Energy* 13(1):30–42.

562 Koue J., H. Shimadera, T. Matsuo, and A. Kondo. 2018. Evaluation of Thermal Stratification and Flow Field
563 Reproduced by a Three-Dimensional Hydrodynamic Model in Lake Biwa, Japan. *Water* 10(47):1–20,
564 doi:10.3390/w10010047

565 Luhar M., and H. M. Nepf. 2011. Flow-induced reconfiguration of buoyant and flexible aquatic vegetation.
566 *Limnology and Oceanography* 56(6), 2003–2017, doi:10.4319/lo.2011.56.6.2003

567 Mei W., and S.-P. Xie. 2016. Intensification of landfalling typhoons over the northwest Pacific since the late
568 1970s. *Nature Geoscience* 9:753–757, DOI: 10.1038/NGEO2792

569 Miller J. W., P. M. Kocovsky, D. Wiegmann, and J. G. Miner. 2018. Fish Community Responses to Submerged
570 Aquatic Vegetation in Maumee Bay, Western Lake Erie. *North American Journal of Fisheries Management*
571 38(3): 623–629, doi.org/10.1002/nafm.10061

572 Nakada S., N. Hirose, T. Senjyu, K. Fukudome, T. Tsuji, and N. Okei. 2014. Operational Ocean Prediction
573 Experiments for Smart Coastal Fishing. *Progress in Oceanography* 121:125–140, doi:
574 10.1016/j.pocean.2013.10.008

575 Nakada S., M. Hayashi, S. Koshimura, Y. Taniguchi, and E. Kobayashi. 2017. Salinization by Tsunami in a
576 semi-enclosed bay: Tsunami-Ocean 3D simulation based on the great earthquake scenario along the Nankai
577 Trough. *J. Adv. Simulat. Sci. Eng.* 3(2):206–214.

578 Nakada S., M. Hayashi, S. and Koshimura. 2018. Transportation of Sediment and Heavy Metals Resuspended
579 by a Giant Tsunami Based on Coupled Three-Dimensional Tsunami, Ocean, and Particle-Tracking
580 Simulations. *Journal of Water and Environment Technology* 16(4):161–174, doi:10.2965/jwet.17-028

581 Nakada S., and Y. Isoda. 2000. Seasonal variation of the Tsushima Warm Current off Toyama Bay. *Umi Sora*
582 76:17–24 [in Japanese].

583 Nakano S., N. Ito, and H. Inoue. 1991. Critical Yield and Shear Stresses for Mud Erosion under Wave. *Proc*
584 *Coast Eng. JSCE* 38:461–465. [in Japanese].

585 Otsubo K., and K. Muraoka. 1985. Physical Properties and Critical Shear Stress of Cohesive Bottom Sediments.
586 *J. Hydraulic, Coastal and Environmental Engineering* 363(II-4):225–234. [in Japanese].

587 Sato Y., E. Komatsu, H. Nagare, H. Uehara, T. Yuasa, T. Okubo, T. Okamoto, and J. Kim. 2011. Construction
588 and Validation of Lake Biwa Basin Simulation Model with Integration of Three Components of Land, Lake
589 Flow, and Lake Ecosystem. *Journal of Japan Society on Water Environment* 34(9):125–141, doi:
590 10.2965/jswe.34.125

591 Schriver P., J. Bøgestrand, E. Jeppesen, and M. Søndergaard. 1995. Impact of submerged macrophytes on fish-
592 zooplankton-phytoplankton interactions: large-scale enclosure experiments in a shallow eutrophic lake.
593 *Freshwater Biology* 33:255–270.

594 Short F. T., S. Kosten, P. A. Morgan, S. Malone, and G. E. Moore. 2016. Impacts of climate change on submerged
595 and emergent wetland plants. *Aquatic Botany* 135:3–17, doi:10.1016/j.aquabot.2016.06.006

596 Sood A., P. L. Uniyal, R. Prasanna, and A. S. Ahluwalia. 2012. Phytoremediation Potential of Aquatic
597 Macrophyte, *Azolla*. *AMBIO* 41:122–137, doi: 10.1007/s13280-011-0159-z

598 Umita T., T. Kasuda, T. Futawatari, and Y. Awaya. 1988. Study on Erosional Process of Soft Muds. *J. Hydraulic,*
599 *Coastal and Environmental Engineering* 398(II-9):33–42. [in Japanese]

600 Yanran D., J. Chenrong, L. Wei, H. Shenghua, and W. Zhenbin. 2012. Effects of the submerged macrophyte
601 *Ceratophyllum demersum* L. on restoration of a eutrophic waterbody and its optimal coverage. *Ecological*
602 *Engineering* 40:113–116, doi:10.1016/j.ecoleng.2011.12.023

603 Weisner S. E. B., J. A. Strand, and H. Sandsten. 1997. Mechanisms regulating abundance of submerged
604 vegetation in shallow eutrophic lakes. *Oecologia* 109:592–599.

605 Wang Q., D. Yu, Z. Li, and L. Wang. 2008. The Effect of Typhoons on the Diversity and Distribution Pattern of
606 Aquatic Plants on Hainan Island, South China. *Biotropica* 40(6):692–699, doi: 10.1111/j.1744-
607 7429.2008.00430.x

608 Wang X., W. Wang, and C. Tong. 2016. A review on impact of typhoons and hurricanes on coastal wetland
609 ecosystems. *Acta Ecologica Sinica* 36:23–29, doi: 10.1016/j.chnaes.2015.12.006

610

611

612

Figure captions

613

614

615 **Figure 1.** Maps of the (a) pressure distribution when Typhoon 21 approached Lake Biwa and the typhoon course
616 (red line and dots), (b) wind vectors and speeds (colors) based on the GPV-MSM reanalysis dataset at 15:00 on
617 4 September, and (c) topography and bathymetry around and in Lake Biwa, respectively. The black and gray
618 squares indicate the gauge stations operated by the Ministry of Land, Infrastructure, Transport and Tourism of
619 Japan (MLIT) and the Lake Biwa Branch Office of the National Institute for Environmental Studies (LaBBO-
620 NIES), respectively. White squares denote the Ogoto offshore comprehensive automatic observation station
621 (OOCAOS) in the south basin of Lake Biwa. (d) Bathymetric maps for the analysis in the south basin. The black
622 solid lines indicate the transect lines for the echosounding observations to measure the vegetation height of the
623 submerged macrophytes.

624

625 **Figure 2.** Conceptual diagrams of the two processes responsible for the vegetation outflow induced by the high-
626 speed current. (a) Erosion (Case 1) evaluated by the nondimensional bed shear stress and the sediment flux from
627 the bed to the lake water. (b) Fluid force (Case 2) represented by the resultant of the buoyancy and drag forces.
628 The variables depicted in the diagram are explained further in the text.

629

630 **Figure 3.** Flowchart of the erosion and fluid force evaluation based on the simulated results of the FVCOM
631 (center gray-shaded square) using the observed datasets (left gray-shaded group) and meteorological reanalysis
632 datasets (upper white square).

633

634 **Figure 4.** Maps of the unstructured triangular grids in the FVCOM for (a) the whole basin of Lake Biwa and
635 (b) the south basin. The total numbers of the triangular cells and nodes are 284,569 and 144,037, respectively.
636 The colors indicate that the horizontal resolution of the grids (measured by the side length of each triangle) is
637 10–60 m and increases up to 10–20 m in the south basin, for example, in (c) Yamanoshita Bay, (d) the Karasuma
638 Peninsula, (e) the Yabase region, and small three islands in the north basin.

639

640 **Figure 5.** Map of the moisture content (%) in the lake bed of the south basin. Colored dots indicate the
641 observational site moisture contents observed in September 2002 (Haga et al., 2006).

642

643 **Figure 6.** Distribution of the macrophyte height (m) in the south basin of Lake Biwa on 9 August 2018, (a) and
644 on 5 September (b). (c) Temporal change in the macrophyte height derived by subtracting the height on 5
645 September (b) from the height on 9 August (a).

646

647 **Figure 7.** Temporal variation of the chlorophyll-a concentration observed at the OOCAOS located in the south
648 basin during the period of 2-5 September.

649

650 **Figure 8.** (a) Vectors of the area-averaged wind speed derived from the hourly GPV-MSM reanalysis dataset in

651 the south basin during the period of 2-6 September 2018. Red shading indicates the date of the Typhoon 21
652 approach around Lake Biwa. (b) Map of the wind vectors and speeds (colors) interpolated using the GPV-MSM
653 reanalysis dataset at 15:00 JST on 4 September. (c) Scatter plots showing the observed and estimated wind
654 speeds during the period of 2-6 September.

655

656 **Figure 9.** (a) Temporal variation reflected in snapshots taken every ten minutes of the observed (colored dots)
657 and simulated (colored lines) water levels at the Mihogasaki (red) and Katayama (blue) gauge stations
658 corresponding to S2 and N2, respectively, as shown in Figure 1. (b) Scatter plots showing the observed and
659 simulated water levels during the period of 14:00-19:00 JST on 4 September. The colors of the dots indicate the
660 eleven gauge stations (N1-N6, S1-S5), as shown in Figure 1.

661

662 **Figure 10.** Snapshots of maps of the simulated water level (color) and surface velocity field (vector) during the
663 period in which Typhoon 21 approached Lake Biwa (14:00-16:00 JST) on 4 September 2018. The inset panels
664 on the bottom right display the observed wind velocities (blue vectors) at each time around Lake Biwa; these
665 data were provided by BiwakoDAS (https://koayu.eri.co.jp/Biwadas_Summary/).

666

667 **Figure 11.** The same as Figure 10 but for the period when Typhoon 21 departed Lake Biwa (17:00-19:00 JST).

668

669 **Figure 12.** Maps of the maximum velocity fields (vectors) and speeds (colors) in the surface (left) and bottom
670 (right) currents simulated by the FVCOM during the period of 14:00-19:00 JST on 4 September 2018.

671

672 **Figure 13.** Simulated time-series of the water level (solid black line), the depth-averaged flow (solid blue line),
673 the surface flow (dashed line), and the bottom flow speed (fine line) averaged over the area of the south basin
674 during the period from 0:00 JST on 4 September to 9:00 JST on 5 September.

675

676 **Figure 14.** Maps of (a) the critical shear stress, (b) the time-averaged bed shear stress, (c) the time-averaged
677 nondimensional bed shear stress, and (d) the time-integrated erosion from the lake bed during the period 0:00-
678 23:50 JST on 4 September.

679

680 **Figure 15.** Maps of the maximum (left) and time-averaged (right) fluid forces acting on the submerged
681 macrophytes during the period of 0:00-23:50 JST on 4 September.

682

683 **Figure 16.** Simulated time-series of the nondimensional bed shear stress (red line) and fluid force acting on the
684 submerged macrophytes (purple line) averaged over the area of the south basin during the period from 0:00 on
685 4 September to 9:00 JST on 5 September.

686

Figures

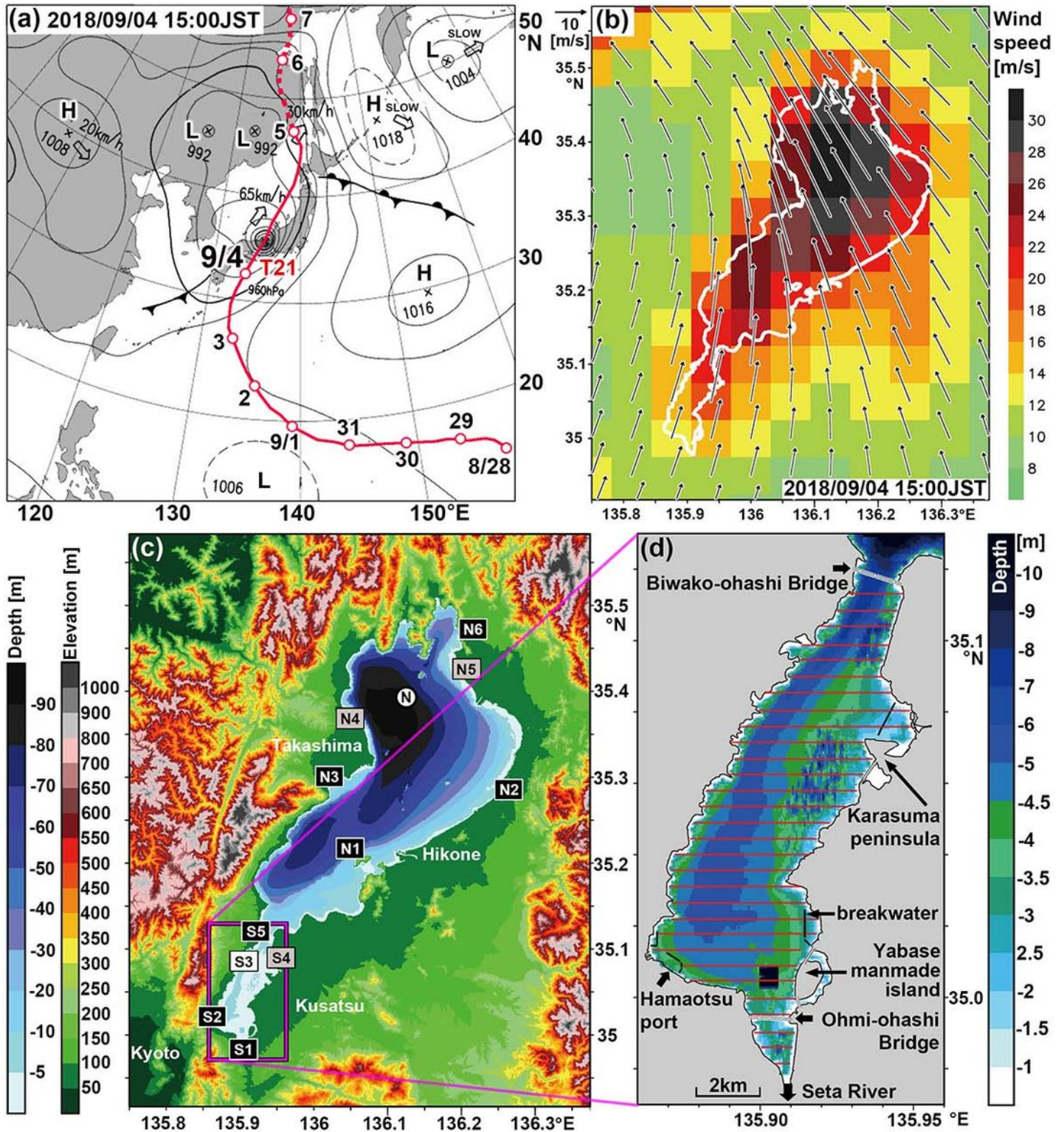


Figure 1

Maps of the (a) pressure distribution when Typhoon 21 approached Lake Biwa and the typhoon course (red line and dots), (b) wind vectors and speeds (colors) based on the GPV-MSM reanalysis dataset at 15:00 on 4 September, and (c) topography and bathymetry around and in Lake Biwa, respectively. The

black and gray squares indicate the gauge stations operated by the Ministry of Land, Infrastructure, Transport and Tourism of Japan (MLIT) and the Lake Biwa Branch Office of the National Institute for Environmental Studies (LaBBO-NIES), respectively. White squares denote the Ogoto offshore comprehensive automatic observation station (OOCAOS) in the south basin of Lake Biwa. (d) Bathymetric maps for the analysis in the south basin. The black solid lines indicate the transect lines for the echosounding observations to measure the vegetation height of the submerged macrophytes. Note: The designations employed and the presentation of the material on this map do not imply the expression of any opinion whatsoever on the part of Research Square concerning the legal status of any country, territory, city or area or of its authorities, or concerning the delimitation of its frontiers or boundaries. This map has been provided by the authors.

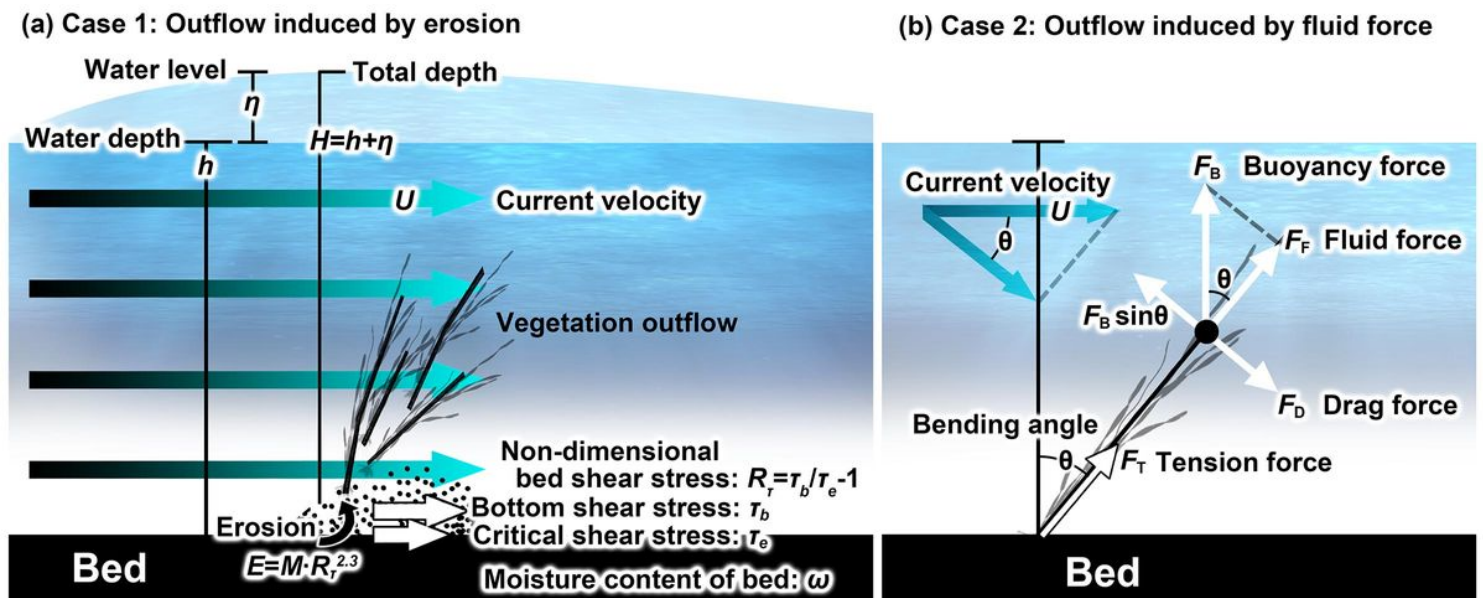


Figure 2

Conceptual diagrams of the two processes responsible for the vegetation outflow induced by the high-speed current. (a) Erosion (Case 1) evaluated by the nondimensional bed shear stress and the sediment flux from the bed to the lake water. (b) Fluid force (Case 2) represented by the resultant of the buoyancy and drag forces. The variables depicted in the diagram are explained further in the text.

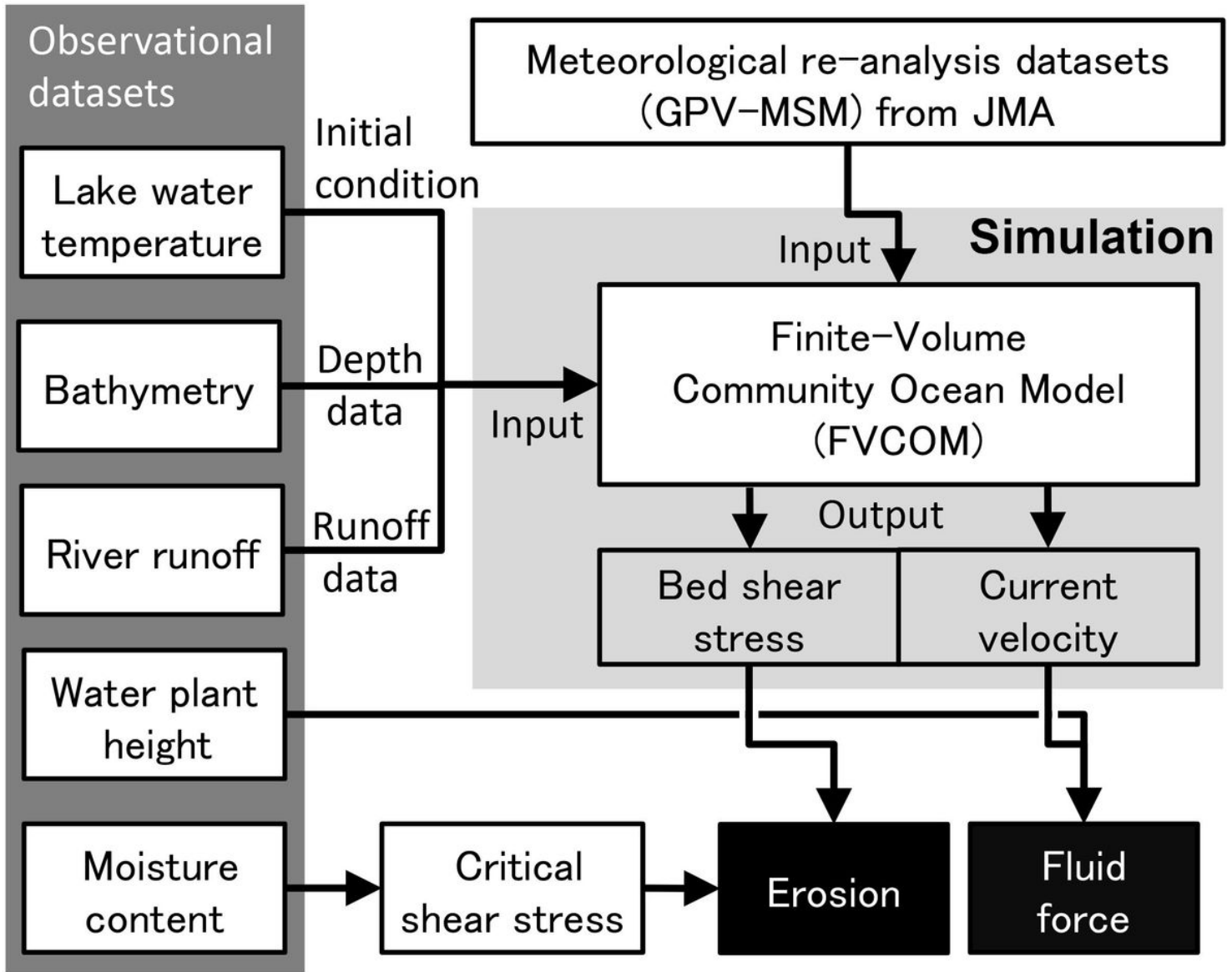


Figure 3

Flowchart of the erosion and fluid force evaluation based on the simulated results of the FVCOM (center gray-shaded square) using the observed datasets (left gray-shaded group) and meteorological reanalysis datasets (upper white square).

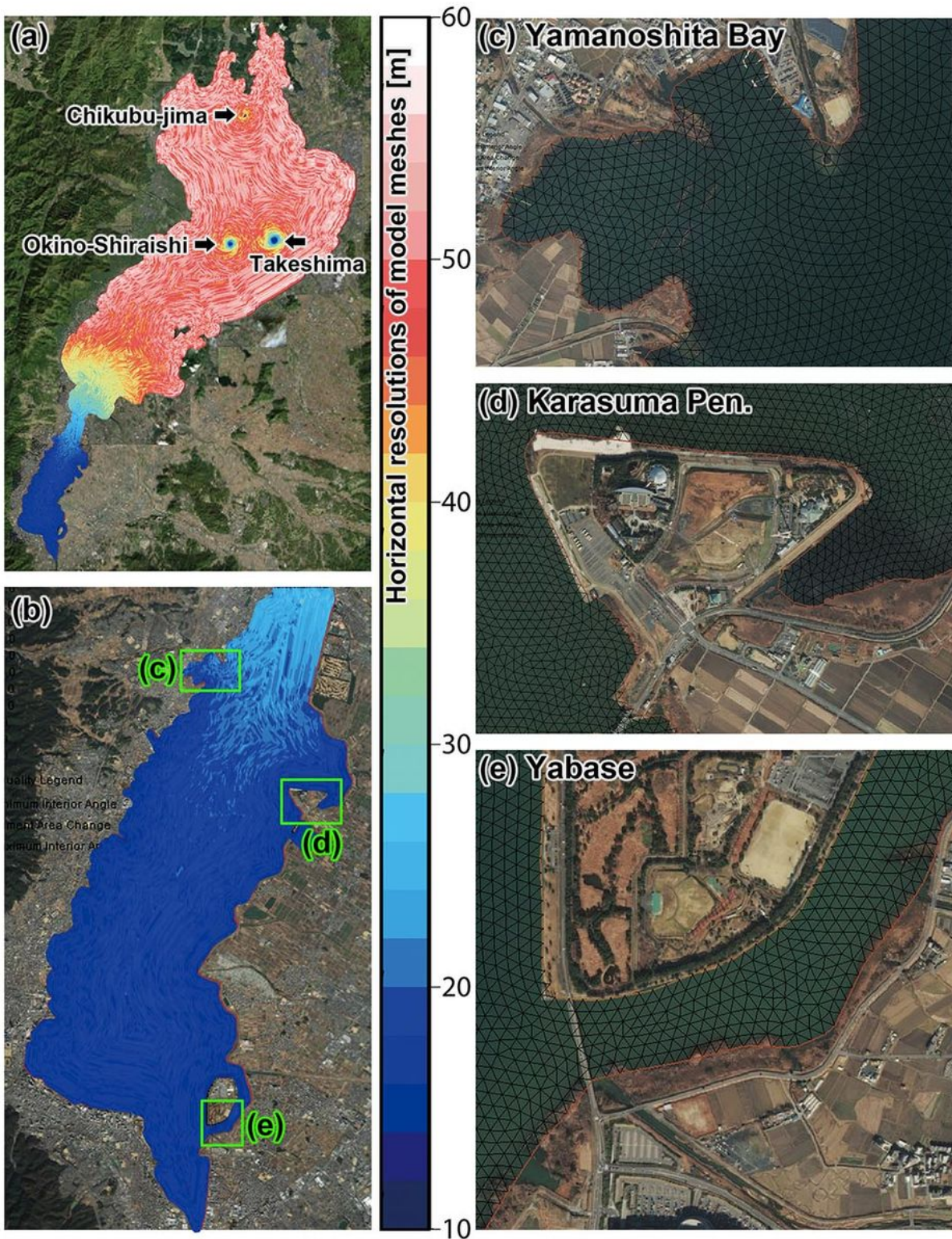


Figure 4

Maps of the unstructured triangular grids in the FVCOM for (a) the whole basin of Lake Biwa and (b) the south basin. The total numbers of the triangular cells and nodes are 284,569 and 144,037, respectively. The colors indicate that the horizontal resolution of the grids (measured by the side length of each triangle) is 10–60 m and increases up to 10–20 m in the south basin, for example, in (c) Yamanoshita Bay, (d) the Karasuma Peninsula, (e) the Yabase region, and small three islands in the north basin. Note:

The designations employed and the presentation of the material on this map do not imply the expression of any opinion whatsoever on the part of Research Square concerning the legal status of any country, territory, city or area or of its authorities, or concerning the delimitation of its frontiers or boundaries. This map has been provided by the authors.

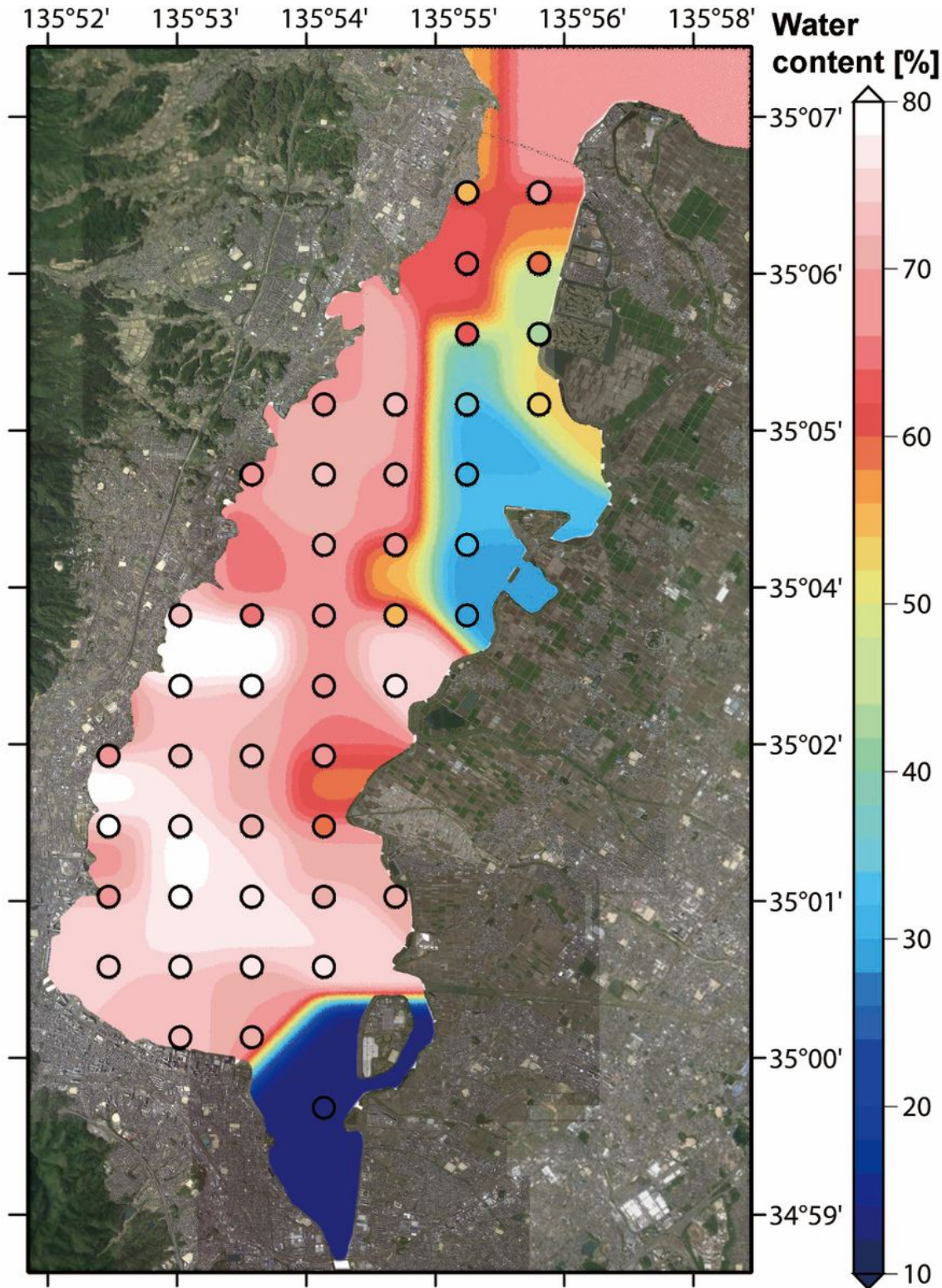


Figure 5

Map of the moisture content (%) in the lake bed of the south basin. Colored dots indicate the observational site moisture contents observed in September 2002 (Haga et al., 2006). Note: The designations employed and the presentation of the material on this map do not imply the expression of any opinion whatsoever on the part of Research Square concerning the legal status of any country, territory, city or area or of its authorities, or concerning the delimitation of its frontiers or boundaries. This map has been provided by the authors.

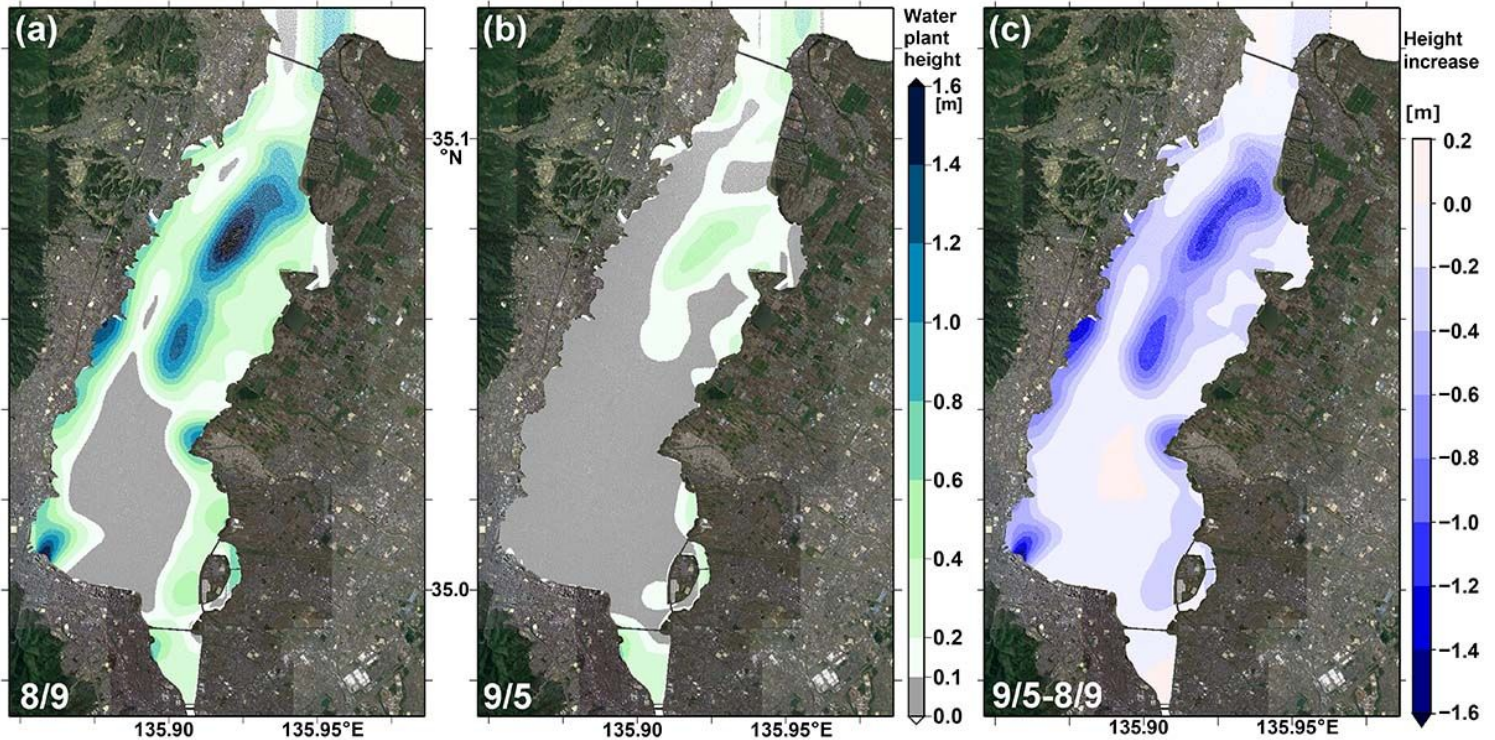


Figure 6

Distribution of the macrophyte height (m) in the south basin of Lake Biwa on 9 August 2018, (a) and on 5 September (b). (c) Temporal change in the macrophyte height derived by subtracting the height on 5 September (b) from the height on 9 August (a). Note: The designations employed and the presentation of the material on this map do not imply the expression of any opinion whatsoever on the part of Research Square concerning the legal status of any country, territory, city or area or of its authorities, or concerning the delimitation of its frontiers or boundaries. This map has been provided by the authors.

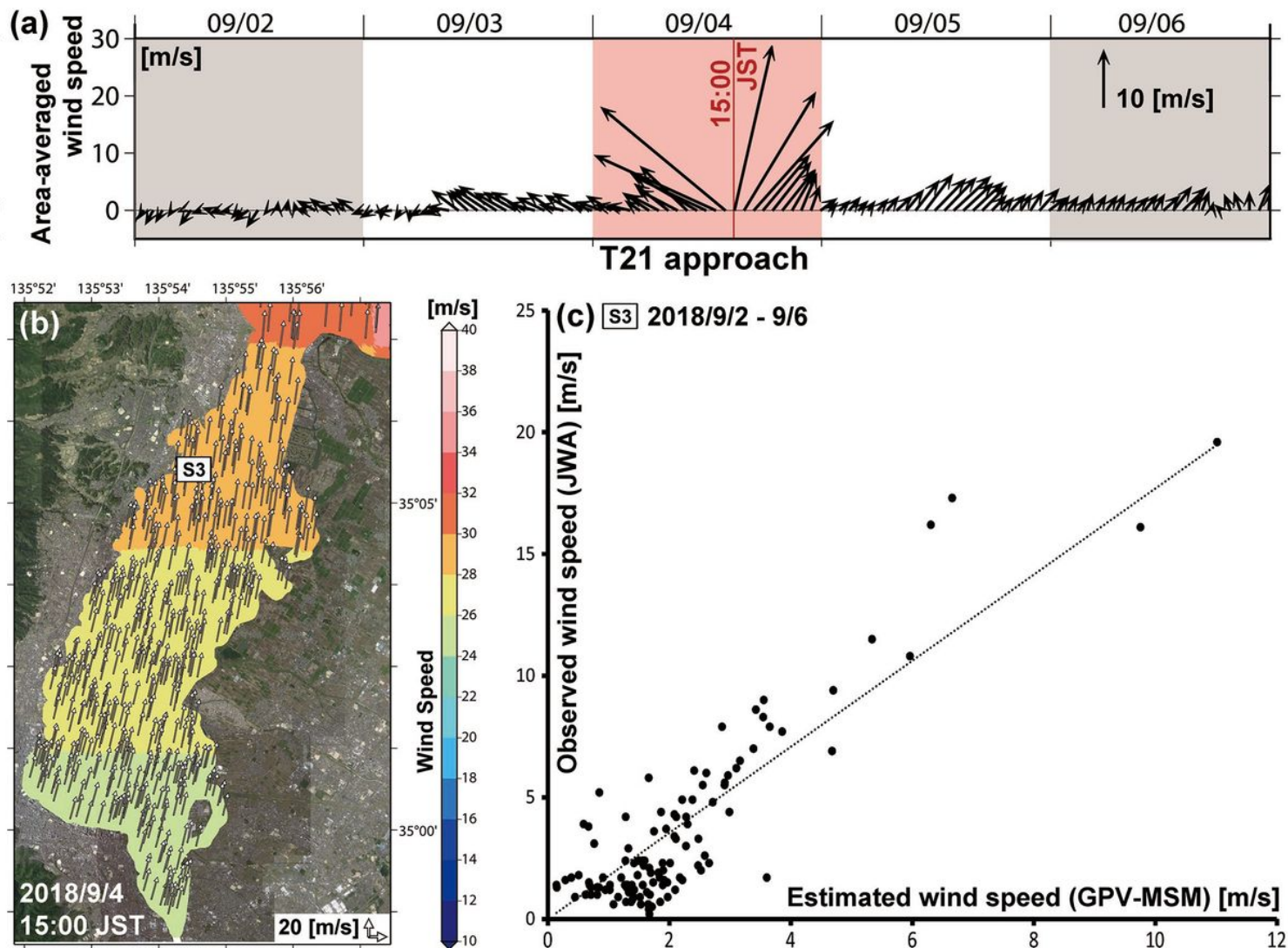


Figure 8

(a) Vectors of the area-averaged wind speed derived from the hourly GPV-MSM reanalysis dataset in the south basin during the period of 2-6 September 2018. Red shading indicates the date of the Typhoon 21 approach around Lake Biwa. (b) Map of the wind vectors and speeds (colors) interpolated using the GPV-MSM reanalysis dataset at 15:00 JST on 4 September. (c) Scatter plots showing the observed and estimated wind speeds during the period of 2-6 September. Note: The designations employed and the presentation of the material on this map do not imply the expression of any opinion whatsoever on the part of Research Square concerning the legal status of any country, territory, city or area or of its authorities, or concerning the delimitation of its frontiers or boundaries. This map has been provided by the authors.

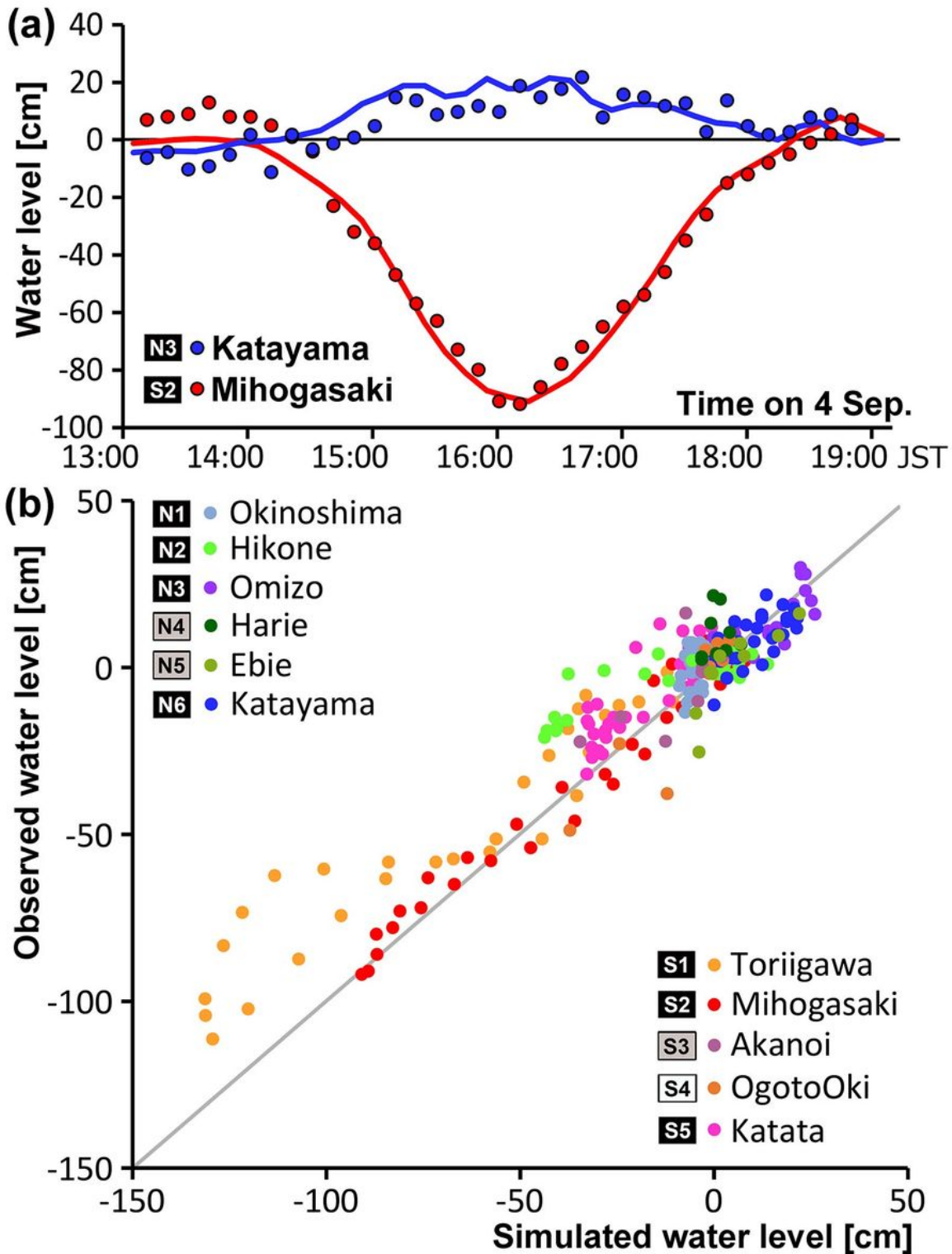


Figure 9

(a) Temporal variation reflected in snapshots taken every ten minutes of the observed (colored dots) and simulated (colored lines) water levels at the Mihogasaki (red) and Katayama (blue) gauge stations corresponding to S2 and N2, respectively, as shown in Figure 1. (b) Scatter plots showing the observed and simulated water levels during the period of 14:00-19:00 JST on 4 September. The colors of the dots indicate the eleven gauge stations (N1-N6, S1-S5), as shown in Figure 1.

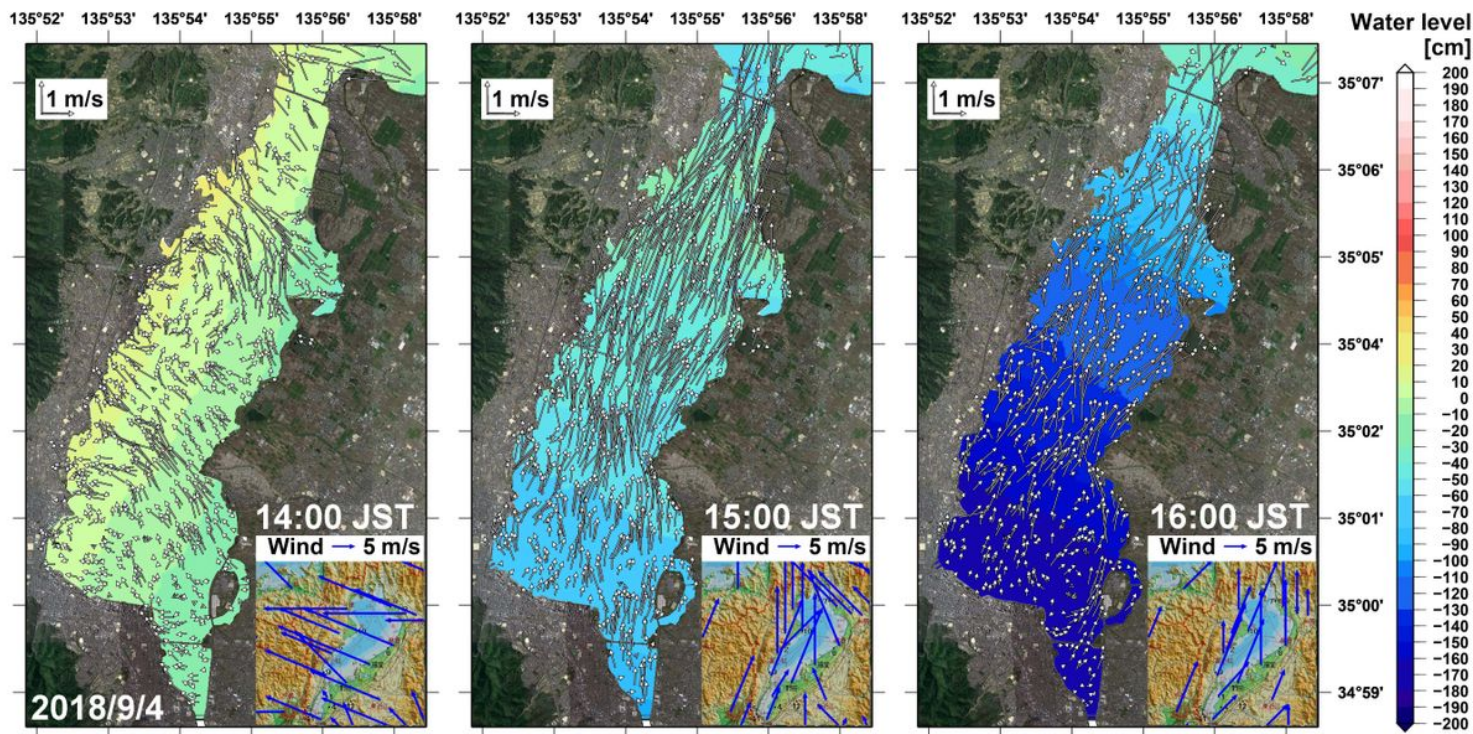


Figure 10

Snapshots of maps of the simulated water level (color) and surface velocity field (vector) during the period in which Typhoon 21 approached Lake Biwa (14:00-16:00 JST) on 4 September 2018. The inset panels on the bottom right display the observed wind velocities (blue vectors) at each time around Lake Biwa; these data were provided by BiwakoDAS (https://koayu.eri.co.jp/Biwadas_Summary/). Note: The designations employed and the presentation of the material on this map do not imply the expression of any opinion whatsoever on the part of Research Square concerning the legal status of any country, territory, city or area or of its authorities, or concerning the delimitation of its frontiers or boundaries. This map has been provided by the authors.

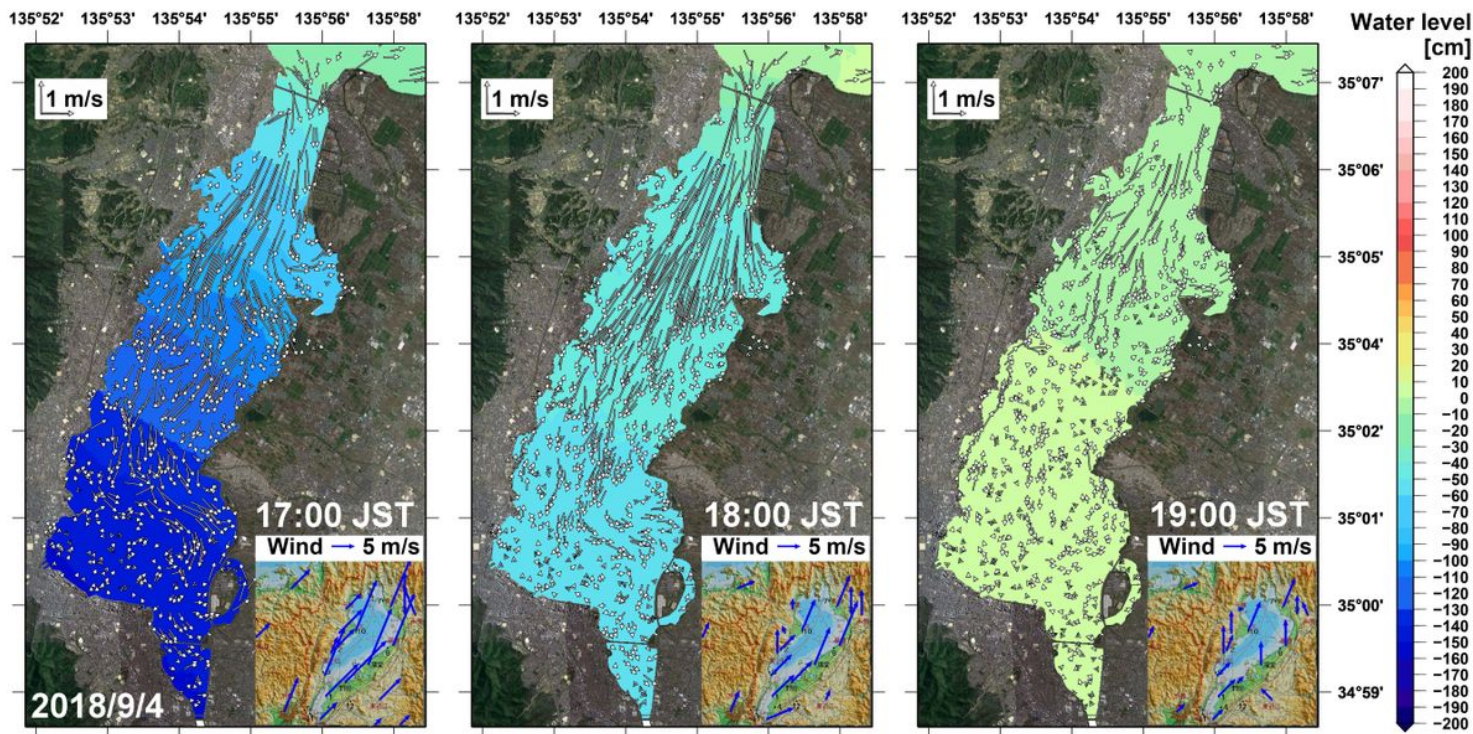


Figure 11

The same as Figure 10 but for the period when Typhoon 21 departed Lake Biwa (17:00-19:00 JST). Note: The designations employed and the presentation of the material on this map do not imply the expression of any opinion whatsoever on the part of Research Square concerning the legal status of any country, territory, city or area or of its authorities, or concerning the delimitation of its frontiers or boundaries. This map has been provided by the authors.

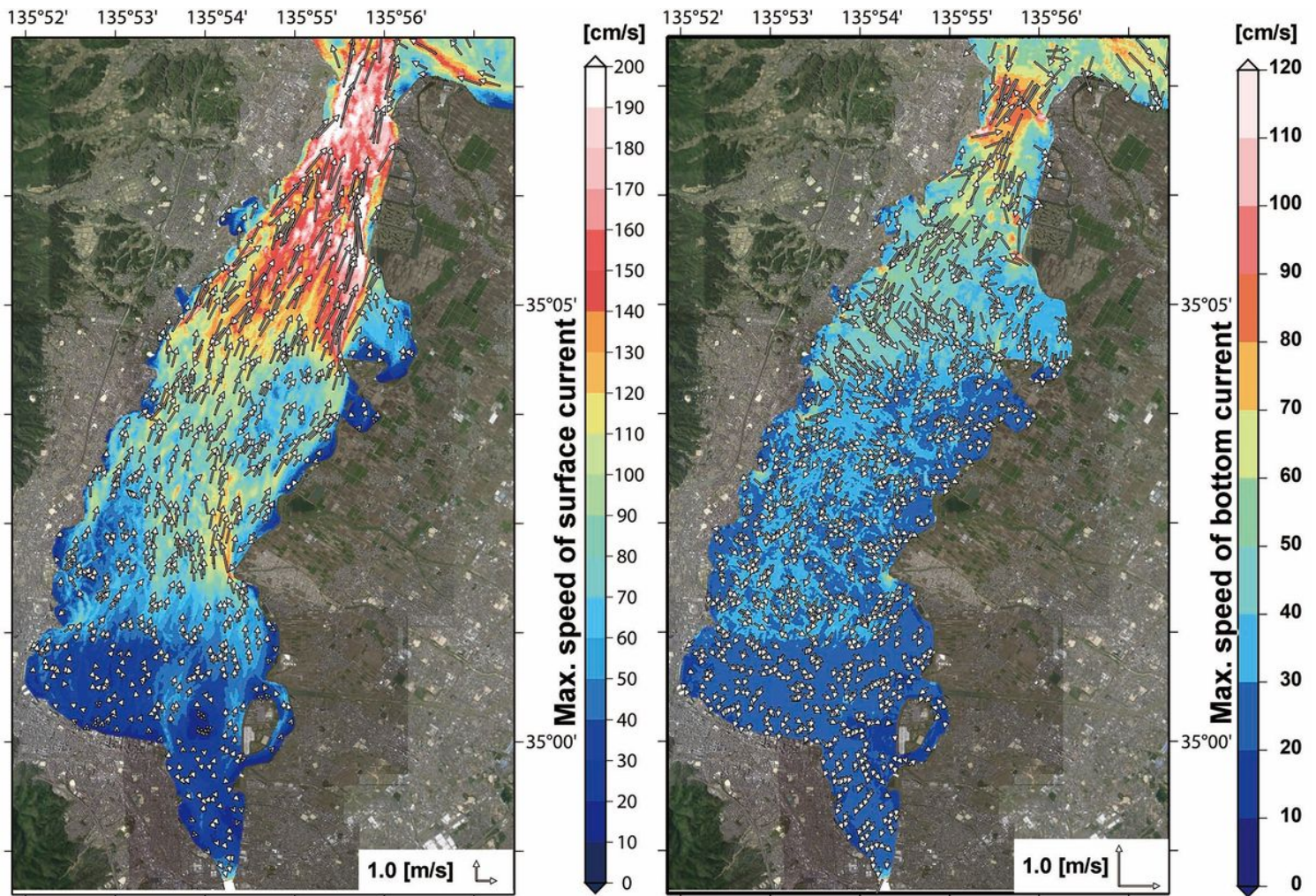


Figure 12

Maps of the maximum velocity fields (vectors) and speeds (colors) in the surface (left) and bottom (right) currents simulated by the FVCOM during the period of 14:00-19:00 JST on 4 September 2018. Note: The designations employed and the presentation of the material on this map do not imply the expression of any opinion whatsoever on the part of Research Square concerning the legal status of any country, territory, city or area or of its authorities, or concerning the delimitation of its frontiers or boundaries. This map has been provided by the authors.

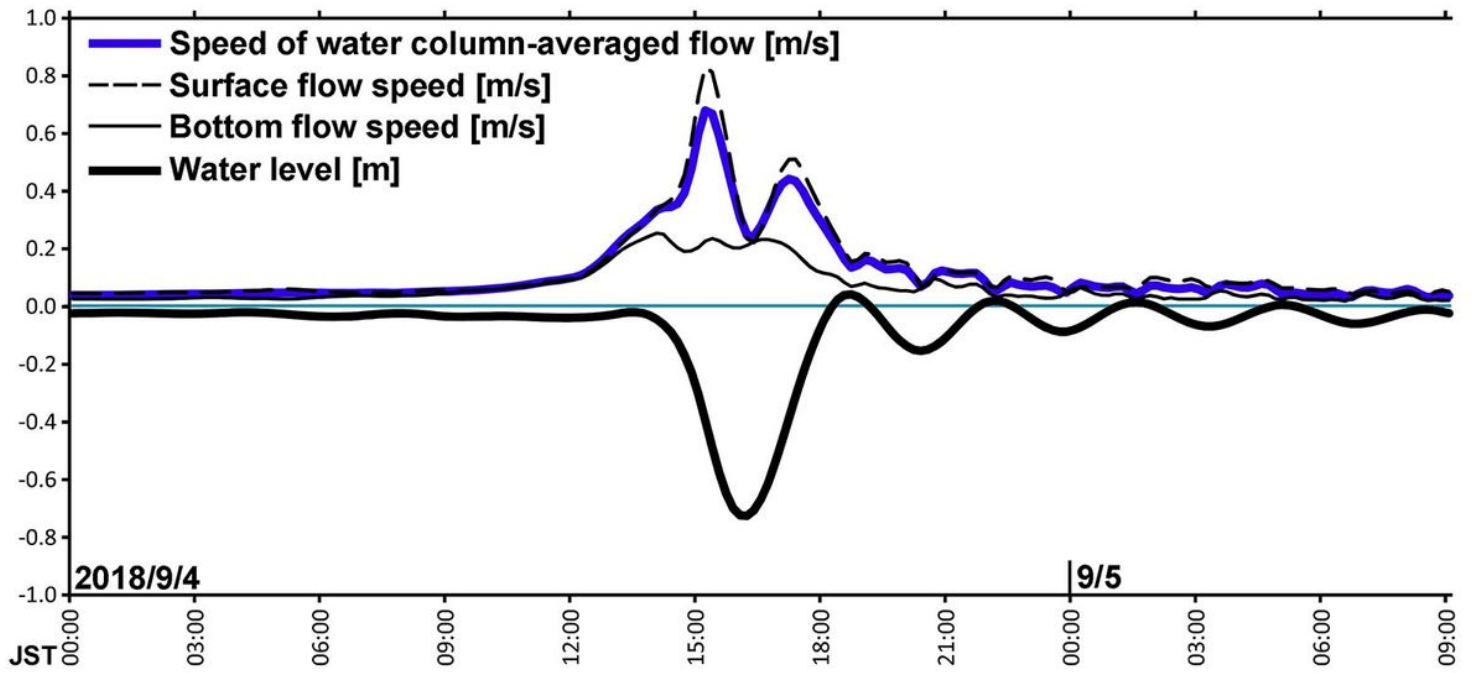


Figure 13

Simulated time-series of the water level (solid black line), the depth-averaged flow (solid blue line), the surface flow (dashed line), and the bottom flow speed (fine line) averaged over the area of the south basin during the period from 0:00 JST on 4 September to 9:00 JST on 5 September.

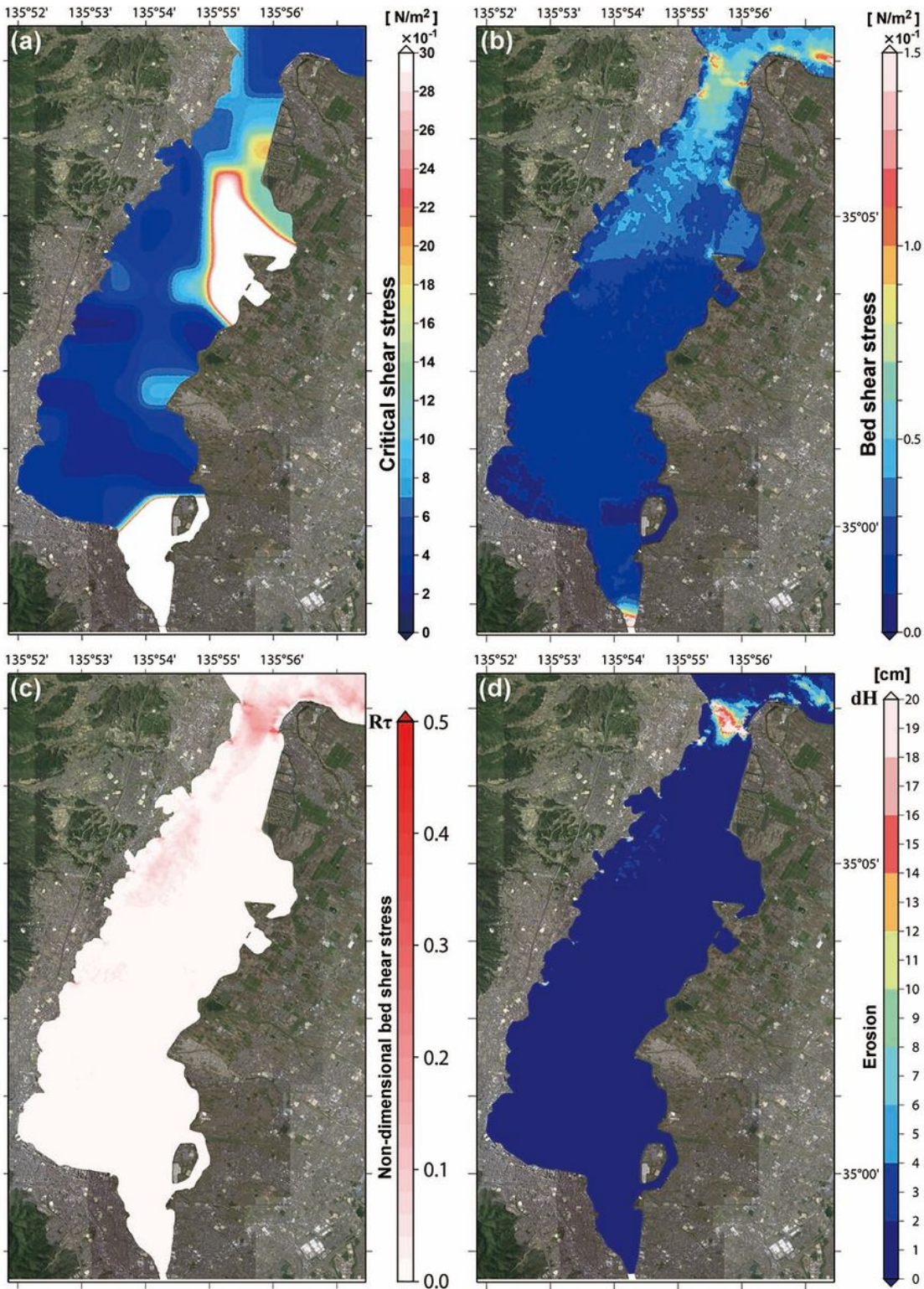


Figure 14

Maps of (a) the critical shear stress, (b) the time-averaged bed shear stress, (c) the time-averaged nondimensional bed shear stress, and (d) the time-integrated erosion from the lake bed during the period 0:00-23:50 JST on 4 September. Note: The designations employed and the presentation of the material on this map do not imply the expression of any opinion whatsoever on the part of Research Square

concerning the legal status of any country, territory, city or area or of its authorities, or concerning the delimitation of its frontiers or boundaries. This map has been provided by the authors.

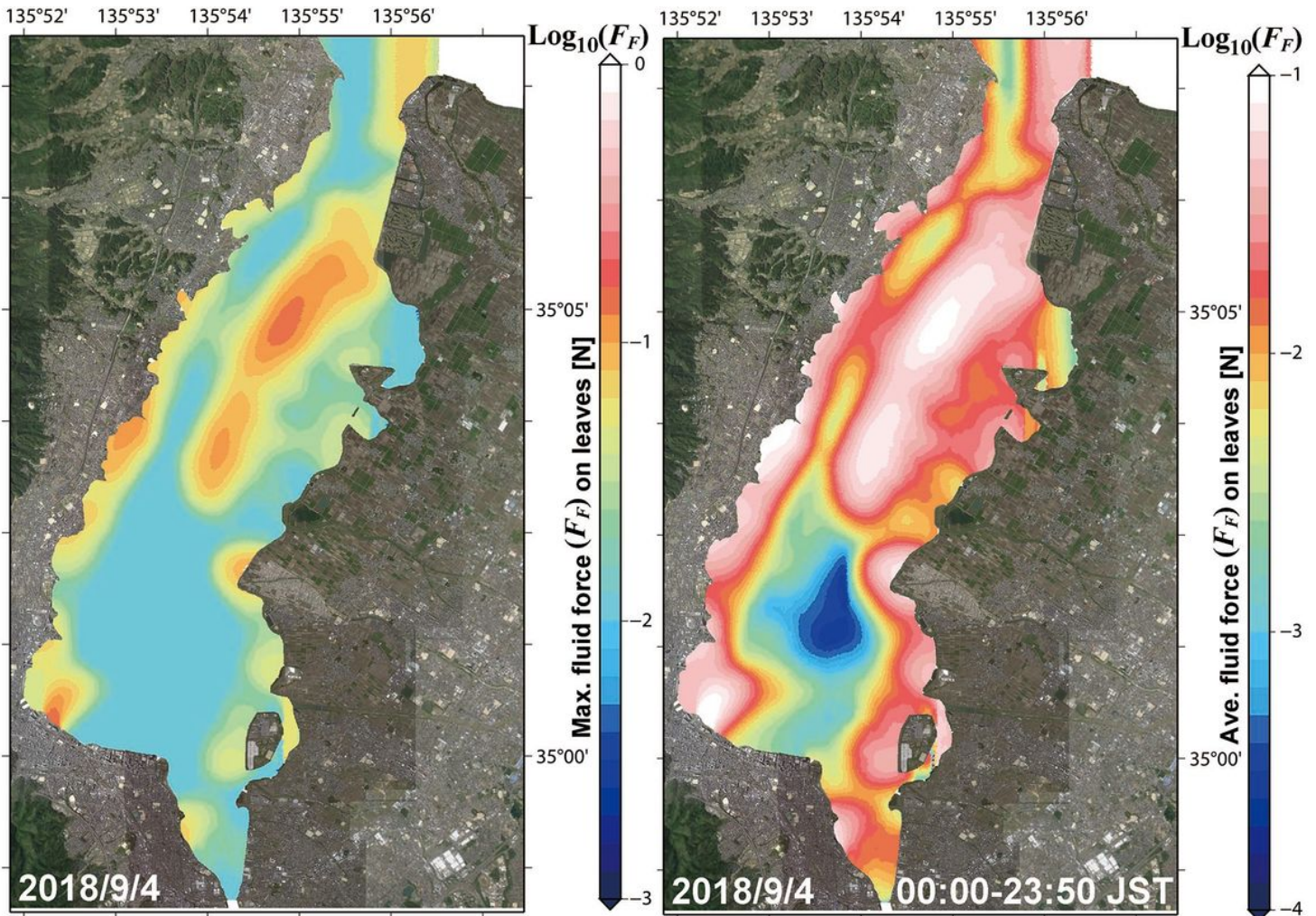


Figure 15

Maps of the maximum (left) and time-averaged (right) fluid forces acting on the submerged macrophytes during the period of 0:00-23:50 JST on 4 September. Note: The designations employed and the presentation of the material on this map do not imply the expression of any opinion whatsoever on the part of Research Square concerning the legal status of any country, territory, city or area or of its authorities, or concerning the delimitation of its frontiers or boundaries. This map has been provided by the authors.

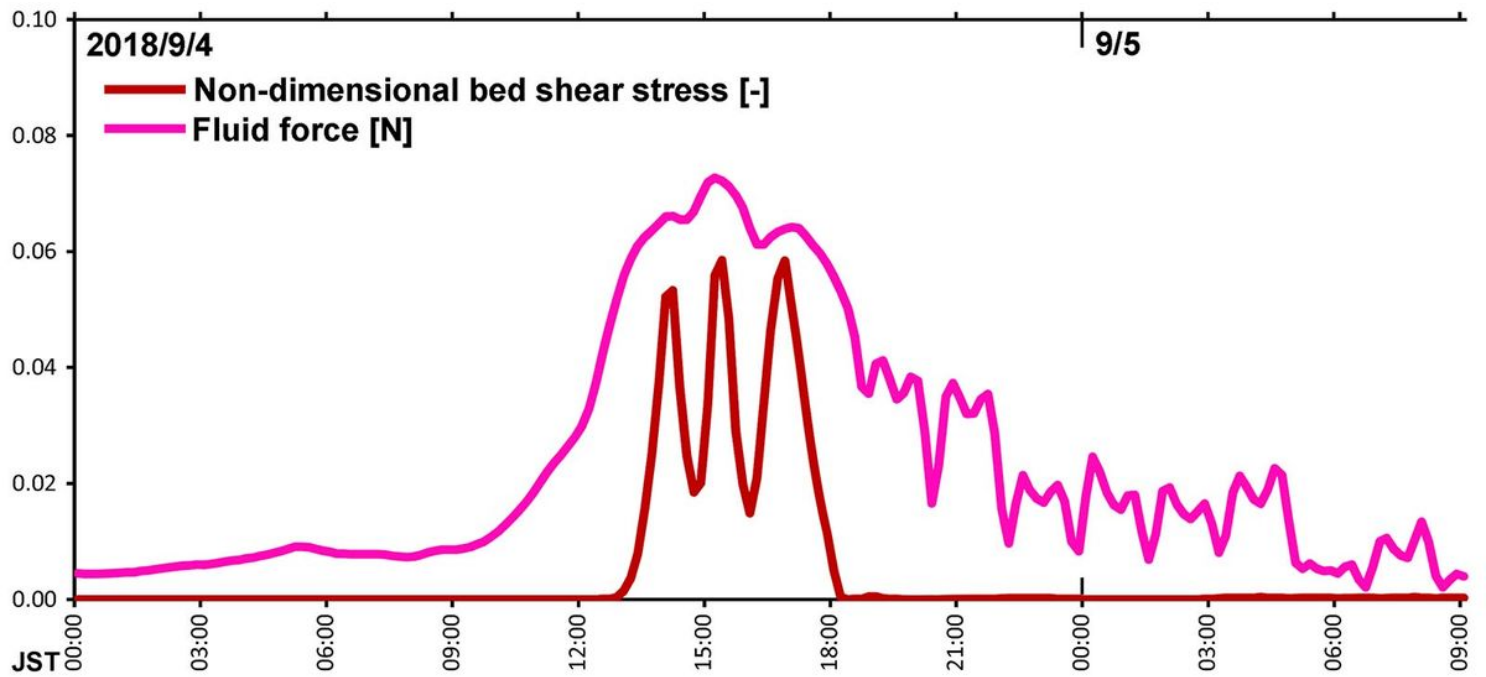


Figure 16

Simulated time-series of the nondimensional bed shear stress (red line) and fluid force acting on the submerged macrophytes (purple line) averaged over the area of the south basin during the period from 0:00 on 4 September to 9:00 JST on 5 September.

Supplementary Files

This is a list of supplementary files associated with this preprint. Click to download.

- [GraphicalAbstractv2.jpg](#)